Solar Energy 316 (2026) 114923

Contents lists available at ScienceDirect

Solar Energy

journal homepage: www.elsevier.com/locate/solener

Comparison of humidity-induced stress levels between floating and ground-mounted photovoltaics

Nathan Roosloot [a,b,*], Dag Lindholm [a], Sayan Adhikari [a], François Clayer [c,1], Curtis L. DeGasperi [d], Blaize A. Denfeld [e], Piet Verburg [f], Huaxia Yao [g], James A. Rusak [g,h], Ankur R. Desai [i], Daniel Hornbach [j], Katy Nugent [k], Ulrike Obertegger [l], Kiyoko Yokota [m], Junhong Wang [n], Torunn Kjeldstad [a], Josefine H. Selj [a], Gaute Otnes [a]

[a] Institute for Energy Technology, Kjeller, Norway
[b] University of Oslo, Oslo, Norway
[c] Norwegian Institute for Water Research, Oslo, Norway
[d] King County, Seattle, United States
[e] Swedish University of Agricultural Sciences, Uppsala, Sweden
[f] School of Geography, Environment and Earth Sciences, Victoria University of Wellington, Wellington, New Zealand
[g] Ministry of the Environment, Conservation and Parks, Ontario, Canada
[h] Department of Biology, Queen's University, Kingston, Ontario, Canada
[i] University of Wisconsin-Madison, Madison, WI, United States
[j] Macalester College, Saint Paul, MN, United States
[k] University of Saskatchewan, Saskatoon, Canada
[l] Fondazione Edmund Mach, S. Michele all'Adige, Italy
[m] Biology Department, State University of New York at Oneonta, United States
[n] University at Albany, Albany, NY, United States

ARTICLE INFO

Keywords:
Finite element method
Floating photovoltaics
Humidity-induced stress
Moisture ingress
Relative humidity
Reliability

ABSTRACT

Floating photovoltaic (FPV) modules operate above water, leading to concerns about increased humidity-induced degradation compared to ground-mounted PV (GPV) modules. However, data to assess FPV degradation are limited. This study addresses this knowledge gap by analysing multi-year meteorological datasets from seven inland water bodies and nearby locations on land and subsequently calculating module temperatures, relative humidities (RH), and moisture ingress profiles. Ambient and module temperatures over water and land were similar (absolute mean differences of under 2 °C), while RHs over water surfaces could be higher or lower than over land (absolute mean differences of up to 9 percentage points), depending on location. Over land, diurnal fluctuations in temperature and RH were higher than over water, attributed to the stabilizing influence of water bodies. Modelled internal moisture contents were almost always higher in GPV modules than in FPV ones (up to 37% higher mean concentration). Lastly, the effects of FPV system design on humidity-induced stress were studied by varying module height above water and system heat transfer efficiency. This led to changes in internal moisture contents (up to 47% and 42% differences in mean moisture concentration, respectively) that often exceeded the observed water-land differences, indicating the importance of FPV system design on humidity-induced stress. This study challenges the commonly held assumption of universally greater humidity-induced stress in FPV systems and highlights the critical role of site-specific factors and system design, thereby advancing the understanding of FPV reliability.

* Corresponding author at: Institute for Energy Technology, Kjeller, Norway.
E-mail address: nathan.roosloot@ife.no (N. Roosloot).
[1] Currently at Norwegian Geotechnical Institute, Oslo, Norway.

https://doi.org/10.1016/j.solener.2026.114923
Received 6 January 2026; Received in revised form 13 July 2026; Accepted 15 July 2026
Available online 20 July 2026

Nomenclature

PV	Photovoltaic
FPV	Floating photovoltaic
GPV	Ground-mounted photovoltaic
FEM	Finite Element Method
GLEON	Global Lake Ecological Observatory Network
ERA5	Fifth-generation ECMWF atmospheric reanalysis
TMY	Typical Meteorological Year
EVA	Ethylene vinyl acetate
POE	Polyolefin elastomer
TOPCon	Tunnel oxide passivated contact
SHJ	Silicon heterojunction
RH	Relative humidity (%)
T_{air}	Ambient air temperature (°C)
T_{water}	Surface water temperature (°C)
T_{mod}	Module temperature (°C)
WS	Wind speed (m/s)
u_0	Wind-independent heat loss coefficient (W/m^{2}C)
u_1	Wind-dependent heat loss coefficient (W/m^{2}C·m/s)
ε	Emissivity of glass
σ	Stefan–Boltzmann constant (W/m^{2}C^4)
F	View factor
α	Module tilt angle (°)
SSRD	Surface solar radiation downwards (J/m^2)
SSR	Surface net solar radiation (J/m^2)
FDIR	Direct solar radiation at surface (J/m^2)
STRD	Surface thermal radiation downwards (J/m^2)
GHI	Global horizontal irradiance (W/m^2)
DHI	Diffuse horizontal irradiance (W/m^2)
DNI	Direct normal irradiance (W/m^2)
G_{poa}	Plane-of-array irradiance (W/m^2)
q_{dr}	Down-welling thermal radiation (W/m^2)
α_H	Hellmann exponent
C	Moisture concentration (g/cm^3)
D	Diffusivity coefficient (cm^2/s)
S	Solubility coefficient (g/cm^3/Pa)
p_v	Partial vapour pressure (Pa)
p_{sat}	Saturation vapour pressure (Pa)
D_0	Pre-exponential diffusivity factor (cm^2/s)
E_D	Activation energy for diffusivity (kJ/mol)
S_0	Pre-exponential solubility factor (g/cm^3/Pa)
E_S	Activation energy for solubility (kJ/mol)
R	Universal gas constant (J/mol·K)

1. Introduction

The floating photovoltaic (FPV) market, where solar modules are installed on buoyant structures floating on a water body, is a niche PV sector that is rapidly growing. The global installed FPV capacity reached 9.1 GW by the end of 2024 [1], marking a greater than 17-fold increase in installations since 2017 [2]. This growth can be attributed to several benefits of FPV over conventional ground-mounted PV (GPV) installations. Most importantly, FPV systems use water surfaces for solar power generation and thus avoid land-use competition, which is particularly relevant for regions where suitable land is scarce or costly [2,3]. A prominent example is coastal areas, which have the highest population densities [4] and are experiencing rapid population growth [5]. Thus, (nearshore) FPV installations in these regions could provide power generation close to high-demand areas [6,7]. Other potential benefits of FPV are lower site preparation costs [2,8], lower rent of water than land [2], and reduced costs of electrical infrastructure in the case of co-location or hybridization with hydropower [9,10] or offshore wind systems [11]. Additionally, FPV can potentially lead to water evaporation reductions by blocking radiative energy [7,12]. Lastly, FPV systems can possibly have lower module operating temperatures compared to GPV [13,14], leading to increased power production and potentially lower degradation rates [15].

Due to these benefits, the FPV market is expected to continue to grow, but market projections vary widely. This is exemplified by the *Trends in Photovoltaic Applications* report series, which changed its forecast of global installed FPV capacity by 2030 from 60 GW in 2023 [16] to under half of that in 2024 [6]. Such a large change reflects considerable unpredictability in the FPV market's future. One likely contributing factor is uncertainty concerning FPV system reliability. This stems from the expectation that FPV systems can encounter significantly different stress levels than GPV ones. However, both qualitative and quantitative information on stress levels and degradation- and/or failure rates on FPV systems is severely limited. This is related to the high competition within the sector, limiting open data sharing. Additionally, it is difficult to generalize information about FPV system reliability because module stresses can vary significantly depending on the FPV system design and the characteristics of the water body. The challenge is compounded by the fact that, as of late 2024, over 75% of FPV capacity was installed in the previous five years [1]. This means that FPV performance data provide limited insight into mid- to end-of-life degradation and failure modes that have yet to emerge. Given these challenges, an alternative approach to build knowledge on FPV module reliability is by using climatic data to assess differences in module stressors for locations over water and on land. Degradation modelling frameworks established for modules in GPV installations which relate key environmental stressors, e.g. irradiance/UV, temperature (variations) and humidity, to degradation metrics or lifetime, can then be used to assess the effects of the stressor differences between GPV and FPV installations on module stress and/or degradation. Examples of these frameworks can be found in [17,18]. Such use will allow evaluation of how far design principles and stress-testing frameworks established for GPV are transferable to FPV, and, if this is not the case, what adjustments may be needed.

One important stressor where such an approach can be relevant is humidity. High relative humidity (RH) around a PV module can lead to moisture ingress into the module, which is known to contribute to several degradation mechanisms, such as delamination [19,20] and corrosion [21,22]. For GPV modules, these mechanisms have been identified as some of the main reasons for mid-to-end-of-life module degradation and failure [23]. This is one likely reason why several large-scale studies on PV field performance have found higher degradation in hot and humid climates compared to cold or moderate climate zones [24,25]. At the same time, tunnel oxide passivated contact (TOPCon) and silicon heterojunction (SHJ) cells, which are expected to become the most popular cell technologies in the coming decade [26], are reported to be particularly sensitive to humidity-induced stress [27,28]. Due to the constant presence of water in the vicinity of FPV modules, it is often assumed that humidity levels around FPV modules are higher than around GPV ones [29–33], potentially leading to increased rates of moisture ingress and associated degradation. This assumption has led to suggestions of using more severe humidity-related accelerated stress tests, including extended IEC tests [34], such as damp heat [35] and humidity freeze [36], as well as pressure cooker tests [35,37] and water immersion [36]. In addition, FPV module designs with low moisture transmission have been suggested [36,38], including those using glass-glass, low permeability encapsulants and edge sealants. However, to what extent such additional measures and their associated costs are warranted remains uncertain, as the validity and generality of the assumption of higher humidity-induced stress is currently unclear.

There are only a few studies [39–41] suitable to test this assumption, as they have compared measured climatic time-series data around a FPV system with those from land or land-based PV systems, including the most important parameters for moisture ingress: humidity and temperature. In [39], only modest differences were observed between the temperature and RH at the FPV system and on land in a temperate climate, but mean differences are not indicated. In contrast, in [40,41], which were in tropical climates, lower temperatures and higher RH values were found around FPV systems compared to nearby land-based systems. For [40], the mean ambient temperature at the FPV system is 1.2 °C lower than on land, while the mean RH is 4.7 percentage points higher. For [41], the mean FPV module temperature is 11 °C lower, while the mean RH is 11 percentage points higher. However, all three studies have significant shortcomings when trying to use their comparisons to draw conclusions on module stress and/or degradation, since this was not their focus. First, by comparing only daytime and/or daily mean values, they miss important information about stress dynamics during nighttime and at shorter timescales. Second, by comparing RH and temperature separately, they miss crucial information on the coupling between the two. This is important as both moisture diffusion and the associated degradation mechanisms are typically thermally activated. Third, there might be seasonal bias in some of the comparisons due to datasets being shorter than a full calendar year. Fourth, the studies only evaluate the ambient temperature and RH, while module temperatures and RH at and/or inside the module determine moisture ingress [42] and degradation [18,43]. And finally, each study considered a single location only, making the results hard to generalize. As a result, there is thus still a fundamental knowledge gap on humidity-induced stress and degradation in FPV and how it compares to that of GPV.

In this work, this knowledge gap is addressed by gathering and analysing multi-year meteorological datasets from seven inland water bodies and nearby on-land locations spread across three different climate zones. All datasets are based on on-site measurements rather than satellite or reanalysis products. This is important because such products cannot resolve local differences between water and nearby land areas. They lack the required spatial resolution, and provide only spatially averaged near-surface conditions. With these datasets, the ambient data are analysed to assess differences in local stressors a PV module can experience when over water compared to on land. Established analytical models are then used to translate the ambient temperature and humidity to parameters at the module level, enabling a more relevant comparison for assessing module stress and degradation. To quantify humidity-induced stress levels, numerical modelling of moisture ingress is used to assess the resulting differences in moisture concentration inside a PV module over its lifetime. In addition, it is examined how stressor and stress differences relate to PV system design, specifically module height above the water and heat transfer efficiency. From these analyses, one can assess how big the effect of placing a PV module on water is on humidity stress levels compared to other factors such as system design, site-specific conditions, or climate zone. As a result, this work advances the understanding of FPV module reliability and provides an important step towards developing FPV-specific module testing protocols and/or material selection criteria - both imperative for the continued growth of the FPV market.

2. Methods

2.1. Module temperature and humidity calculation

Time series of measured air temperature (T_{air}), RH, and wind speed (WS) above inland water bodies and nearby on-land locations, as well as surface water temperature (T_{water}) for selected sites, together hereafter referred to as on-site measured data, were collected via an open solicitation to the Global Lake Ecological Observatory Network (GLEON). GLEON is one of the primary international networks for sharing of long-term, high-quality in situ measurements at water bodies. Given the importance of removing seasonal bias in the data, sites were required to have at least one year of data in all seasons. This resulted in seven of the participating GLEON sites being suitable for this study, which happened to all be present in relatively cold climates (Fig. 1). The number of available sites reflects the limited global availability of sites that met the study requirements. Throughout the work, the sites will be referred to by the abbreviations indicated in Fig. 1. Their relevant metadata are given in Table 1. None of the sites had PV systems installed on them, except in some cases where individual modules powered the measurement equipment.

Time series of module temperature (T_{mod}) and RH at the module were calculated using the on-site measured data in combination with relevant irradiance data from the fifth generation ECMWF atmospheric reanalysis of the global climate (ERA5) [44] at the respective locations. Reanalysis data were used for irradiance as this was not measured on all sites. In contrast to T_{air}, RH and WS, irradiance is less sensitive to spatial averaging and to whether the surface is water or land, making the use of reanalysis data appropriate. The ERA5 dataset was chosen over the combination of multiple satellite products to ensure spatial and temporal consistency across the study's geographically diverse sites. Module temperatures were calculated from the on-site measured and irradiance data using the Faiman model with a radiative loss term [45]:

$$T_{mod} = T_{air} + \frac{G_{poa} - F\cdot\varepsilon\cdot\left(\sigma\cdot T_{air}^4 - q_{dr}\right)}{u_0 + u_1\cdot WS} \tag{1}$$

where G_{poa} is the plane-of-array irradiance, F is the view factor, which can be expressed in terms of the module tilt angle α via $F = \frac{1+3\cdot cos\alpha}{4}$, ε is the emissivity of glass, which is assumed to be 0.88, σ is the Stefan-Boltzmann constant, q_{dr} is the down-welling thermal radiation, and u_0 and u_1 are the wind-independent and wind-dependent components, respectively, of the heat loss coefficient, often referred to as the U-value.

U-values are a measure of how effectively the system transfers heat with its surroundings (while attempting to exclude the effects of the local climate). U-values of 20.74 W/m^{2}C for u_0 and 2.91 W/m^{2}C·m/s for u_1 were used for both water and land to ensure a consistent comparison between FPV and GPV. These values were previously found with the module temperature model used in this work [45]. However, as previously mentioned, lower operating temperatures are an often-reported benefit of FPV systems over GPV ones. Higher U-values indicate more efficient heat transfer between the system and the environment, thus leading to lower operating temperatures. As both the RH at the module and moisture ingress and related degradation mechanisms are temperature dependent, a temperature lowering for the FPV compared to the GPV system affects the comparison of humidity-induced stress and degradation.

To illustrate the order of magnitude of the effect of higher U-values on module temperature and RH over water, module temperature and RH are re-evaluated for all sites under elevated U-values in Section 3.4.(ii). Several studies have calculated U-values for FPV systems, with overviews provided in [14,15]. The re-evaluation in this study was based on the U-values from [46], which were the highest values reported in the aforementioned overviews. However, the U-values from [46] were determined using a different temperature model that did not include radiative losses and were therefore adapted to align with the temperature model employed in this work. This resulted in the increased U-values used in Section 3.4.(ii) being 45 W/m^{2}C for u_0 and 10 W/m^{2}C·m/s for u_1.

After the module temperature has been determined via Eq. (1), the RH at the module was calculated as well [47]:

$$RH(T_{mod}) = RH(T_{air})\cdot\frac{p_{sat}(T_{air})}{p_{sat}(T_{mod})} \tag{2}$$

where $RH(T_{mod})$ is the RH at the module temperature, representing the

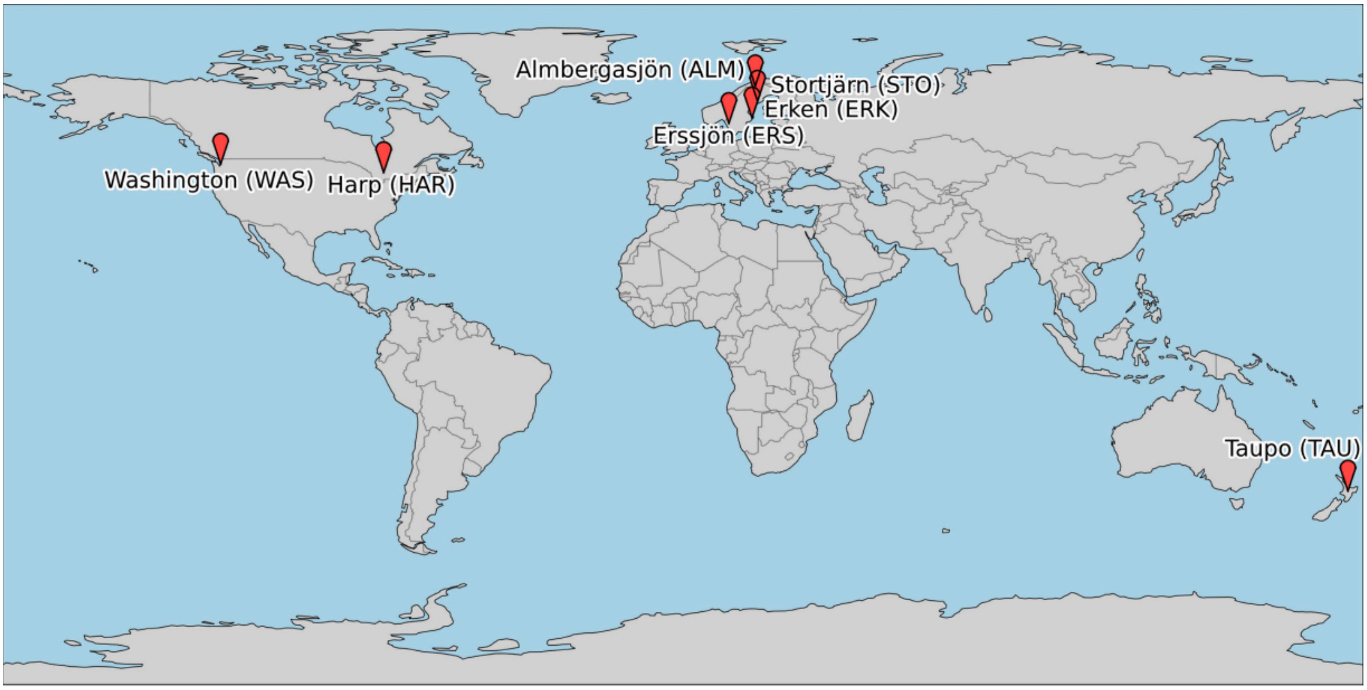

Fig. 1. World map with locations of the sites analysed in this study. Taupo has two sites on land, one south and one northeast of the lake, that are treated as separate comparative cases: Taupo_S (TAU_S) and Taupo_NE (TAU_NE).

RH at the outer module surface, $RH(T_{air})$ is the RH in the ambient air, and $p_{sat}(T_i)$ is the saturation pressure at temperature T_i. The saturation pressure is solely a function of temperature and is in this work calculated using the 1996 Arden-Buck equation [48]. Eq. (2) allows for $RH(T_{mod})$ to exceed 100%, which is when moisture condensation occurs. In these cases, values were capped at 100%. The effects of liquid water are not considered in this work.

The use of a temperature model with a radiative loss term allows for more accurately modelled module temperatures during low or no irradiance, compared to simpler temperature models typically used for performance analysis [45]. This is important for a more precise stressor quantification as radiative losses can lead to module temperatures that are lower than the ambient air temperatures. Eq. (2) shows that this corresponds to higher RH at the outer module surface compared to the ambient.

2.2. Data processing

The section details how the on-site measured data and the irradiance data were processed and combined to create time series of module temperature and RH at hourly resolution. An overview of this process is given in Fig. 2.

The surface solar radiation downwards (SSRD), the total sky direct solar radiation at the surface (FDIR), the surface net solar radiation (SSR), and the surface thermal radiation downwards (STRD) made up the acquired irradiance data from ERA5. All data were at hourly resolution and represented the total accumulated radiation during the hour. By dividing by 3600 and placing the time stamp in the middle of the hour, the data represented the average irradiance during the hour. This yields the mean hourly global horizontal irradiance (GHI) from the SSRD and the mean hourly down-welling thermal radiation (q_{dr}) from the STRD. From the FDIR, one then gets the mean hourly direct irradiance on a horizontal plane. This was transformed to the direct normal irradiance (DNI) by dividing by the cosine of the solar zenith angle. This angle was determined using the NREL SPA algorithm [49], as implemented by the python library pvlib (version 0.10.4) [50]. To avoid unphysical values for the DNI, the DNI was set to 0 for solar zenith angles larger than 87°, which is done by default in most DNI estimation models in pvlib. The diffuse horizontal irradiance (DHI) was calculated by subtracting the FDIR from the GHI. Lastly, the albedo was calculated at each timestamp via $albedo = (SSRD - SSR)/SSRD$, per instruction of the ERA5 documentation [44]. For timestamps where the SSRD was zero or where the found albedo was negative, the albedo was set to 0.

With the GHI, DHI, DNI and albedo as input, the irradiance in the module plane of array (G_{poa}) was calculated using the Perez transposition model [51–53] in pvlib. Other necessary inputs for the Perez transposition model are the solar position at each timestamp and the module azimuth and tilt. The solar position was determined with the same algorithm as previously used for the determination of the solar zenith angle in the DNI calculation. The module azimuth was assumed to be south-facing (180°) for sites in the northern hemisphere, and north-facing (0°) for sites in the southern hemisphere. The module tilt (see Table 1) was the optimized angle for maximum annual energy production in each location as determined by PVGIS version 5.2 using the ERA5 solar radiation database [54]. To make water and land cases at a single site as comparable as possible, the same module tilt angle was used for both. This was despite the fact that for some sites, the optimal module tilt for the location over water differed marginally (maximum 1°) from the one on land, and that the optimal tilt angles over water exceeded typical FPV module tilt angles [55].

To be consistent with the irradiance data, on-site measured data were also used at hourly resolution, with the timestamp in the middle of the hour. As shown in Table 1, for most sites, on-site measured data were already at hourly resolution, with the values representing the average over the hour. For some sites, on-site measured data were instantaneous values at hourly resolution, with values at other instances than in the middle of the hour. In these cases, the data were transformed to the middle of the hour via linear interpolation. Sub-hourly data were only aggregated to hourly data after filtering, as described later.

For several sites, the height at which the wind speed was measured above water or land differed from the heights of the air temperature and RH measurements (see Table 1). To ensure measurements of all on-site measured parameters at the same height, the wind speed measurements were corrected to the same height as that of the air temperature

Table 1
Metadata of included GLEON sites. Coordinates are latitude and longitude, given in decimal degrees. Köppen-Geiger climate zone was calculated based on the coordinates of the land station using [74].

Sitename	Coordinateswater(°)	Altitudewater(m)	Coordinatesland(°)	Altitudeland(m)	K − Gclimatezone	Lakearea(km^2)	Max/Meanlakedepth(m)	MeasurementheightRH&Twater(m)	MeasurementheightWSwater(m)	MeasurementheightRH&Tland(m)	MeasurementheightWSland(m)	Datatypeon − sitemeasureddata	Originaltimeresolutionon − sitemeasureddata	Timezone(UTC + / − Xh)	Timeseriesduration(years)	Missingdata(%)	Moduletilt(°)	Distancelandstationtonearestlakeshore(km)	Comments
Lake Taupo_NE (TAU_NE)	-38.8, 176.0	356	-38.7, 176.1	402	Cfb	620	163/92	2	2	1.2	10	Water RH and T instantaneous, rest hourly average	Hourly	+12	7	19.8	36	1.1	Two measurement stations on land treated as separate cases.
Lake Taupo_S (TAU_S)	-38.8, 176.0	356	-39.0, 175.8	360	Cfb	620	163/92	2	2	1.2	10	Water RH and T instantaneous, rest hourly average	Hourly	+12	7	30.0	36	2.2	See comment Lake Taupo_NE. Water T measurements also used since this site used for the Lake Heat Flux Analyzer.
Harp Lake (HAR)	45.4, -79.1	327	45.2, -78.9	316	Dfb	0.7	38/13	1.75	1.75	2	10	Hourly average	Hourly	-4	2	1.3	39	22.7	Many other lakes between water and land station.
Washington Lake (WAS)	47.6, -122.3	5	47.4, -122.3	113	Csb	88	65/33	3	3	1.2	1.2	Water average of 5 min interval, land RH and T instantaneous , land WS average of 2 min interval	Hourly	-8	15	2.8	40	9.0	Height of air T and WS measurements over land estimated based on photographs.
Erssjön (ERS)	58.4, 12.1	73	58.4, 12.2	80	Dfb	0.06	5/2	1.5	1.5	2.2	2.2	30 min average	30 min	+1	2	9.9	46	0.8	
Erken (ERK)	59.8, 18.6	13	59.8, 18.6	15	Dfb	24	21/9	2	10	1.6	10	Water RH and T instantaneous, water WS 10 min average, land hourly average	Hourly	+1	6	14.9	47	0.4	Water station on small island on lake.
Stortjärn (STO)	64.3, 19.8	284	64.2, 19.8	180	Dfc	0.04	7/3	1.4	1.51	1.7	10	Water 30 min average, land 10 min average	Water 30 min, land 10 min	+1	6	13.3	49	3.2	
Almbergasjön (ALM)	68.3, 19.2	380	68.4, 19.0	351	ET	0.06	6/3	2.3	2.3	2.5	2.2	Water 10 min average, land 30 min average	Water 10 min, land 30 min	+1	2	7.6	48	5.0	Water station at lake shore,both water and land station next to larger lake.
Bangkok (BAN)	-	-	13.7, 100.5	10	Aw	-	-	-	-	2	10	Hourly average	Hourly	+7	1	0	17	-	Land data are TMY. RH height not given, but assumed to be 2 m (equal to T). Constant albedo of 0.25 assumed.

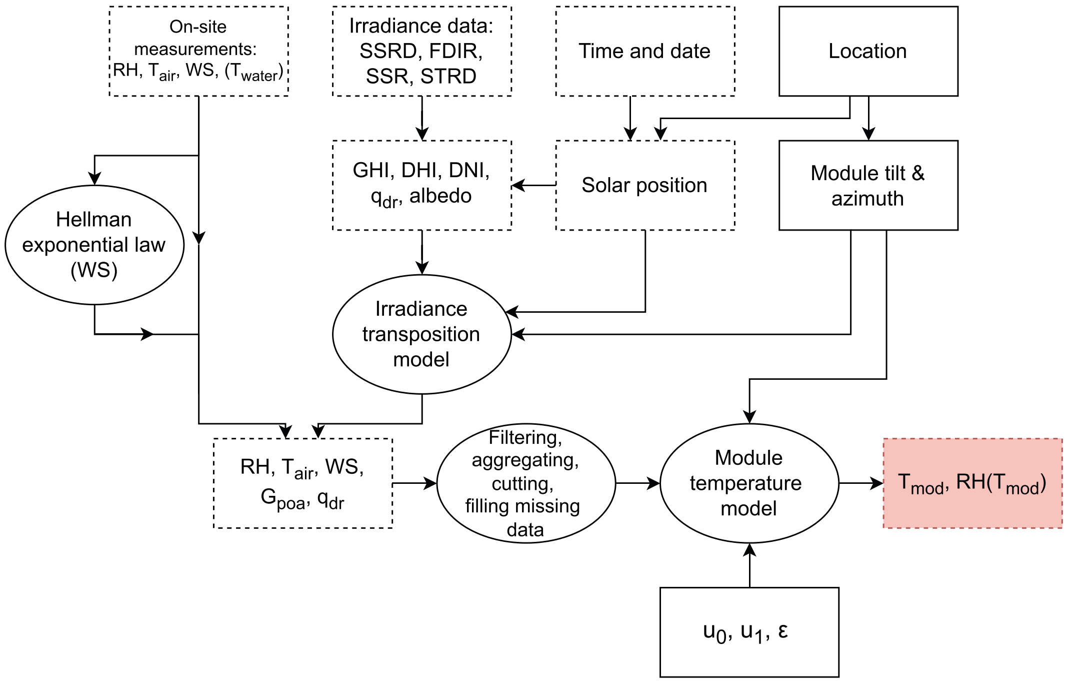

Fig. 2. Flowchart of the data processing steps to go from time series of on-site measurements and irradiance data to module temperature and RH. Rectangles indicate data, while ovals indicate data processing operations. Dotted rectangles indicate time series data. Definitions for abbreviations used in the figure can be found in the main text.

and RH measurements using the Hellmann exponential law [56]:

$$WS_{h_1} = \left(\frac{h_1}{h_2}\right)^{\alpha_H} \cdot WS_{h_2} \tag{3}$$

where WS_{h_i} is the wind speed at height h_i, and α_H is the Hellmann exponent. This exponent was set to 0.2 for measurements over land [57] and 0.1 for measurements over water [56].

After correcting the wind speed values, the on-site measured data of the respective sites were merged with the irradiance data (G_i) at the corresponding timestamps. Following the removal of duplicate timestamp records, outlying values were filtered out based on the physical limits specified in [58]. Firstly, for the data at higher resolution than 15 minutes, measurements were removed if the air temperature changed by more than 4 °C or if the wind speed changed by more than 10 m/s between consecutive datapoints. Secondly, all datapoints outside of the following physical limits were removed: $0 \leq G_i \leq 1300$ W/m^2, $-40 \leq T_{air} \leq 60$ °C, $0 \leq RH \leq 100\%$, $0 \leq WS \leq 32$ m/s. Lastly, visual inspection of the data was applied to confirm that no more outliers were present. To preserve the physical relationship between the different variables, all variables were removed for each timestamp at which a single variable was missing or filtered out.

After filtering, sub-hourly data were aggregated to hourly values with the timestamps in the middle of the hour. Leap days were removed from the data. To avoid seasonal bias in the data, the time series were cut to span full calendar years. The length of the time series and the proportion of missing data for the respective sites are given in Table 1. To further mitigate seasonal bias, missing data were filled according to a method specified in IEC 61724-1 [59], whereby each missing value was imputed with the mean value from the same day-of-year and hour-of-day across all other available years of the timeseries for that parameter. The timeseries of mean data at each unique timestamp in the year will from hereon be referred to as the mean annual cycle. For some sites, the mean annual cycle also contained missing values, meaning that in the original time series, no data were present at any of the years at the given day-of-year and hour-of-day. As with the original time series, all measurements were removed at timestamps with any missing data in the mean annual cycle. They were filled by linear interpolation for gaps of up to two consecutive hours, and by repeating values from the corresponding hours of the previous day for gaps longer than 2 hours.

The resulting time series were on-site measured and irradiance data spanning full calendar years without missing data. From this, the module temperature and RH were calculated using Eqs. (1) and (2), respectively. It was confirmed that no module temperatures were outside the physical limits of $-40 < T_{mod} < 100$ °C as set by [58].

2.3. Moisture ingress modelling

As a means of quantifying humidity-induced stress based on the time series of module temperature and humidity from Section 2.2, moisture ingress into a PV module was modelled for selected sites. Diffusion of moisture was assumed to be Fickian, meaning that the materials' diffusivity coefficient D is independent of the moisture concentration C. Under this assumption, moisture transport is described by Fick's second law:

$$\frac{\partial C}{\partial t} = D \cdot \nabla^2 C \tag{4}$$

This law assumes a continuous concentration, which is not valid at interfaces between dissimilar materials, restricting its use to homogeneous domains only [60]. In PV modules, which often consist of dissimilar materials like backsheets and encapsulants, modelling of moisture ingress with Fick's second law therefore requires additional boundary conditions to impose moisture concentration discontinuities at the interfaces. This is done by assuming that the two sides of each interface (either internal solid-solid or external air-solid) are in equilibrium, meaning that the partial vapour pressure p_v is continuous across it [61]. Assuming that Henry's law,

$$C = S \cdot p_v \tag{5}$$

where S is the solubility coefficient, applies to all materials in the module, the equilibrium condition at the internal boundary between materials 1 and 2 then becomes

$$\frac{C_1}{S_1} = \frac{C_2}{S_2}$$

Similarly, the application of continuous p_v and Henry's law allows the moisture concentration at the outer module boundary C_o to be determined from the p_v in the adjacent air. Given that $p_v = p_{sat}(T)\cdot RH(T)$, this concentration then depends on the solubility of the bordering material, the module temperature, and the RH at the outer module surface:

$$C_o = S\cdot p_{sat}(T_{mod})\cdot RH(T_{mod})$$

Other assumptions in the model were that temperature was uniform across the module and that the inflow on one side of an internal boundary was equal to the outflow on the other side.

Using Eq. (4), three-dimensional moisture ingress was simulated using the finite element method (FEM) with the in-house developed software SiSim [62]. Ingress was simulated for two different module architectures with differing resistance to moisture ingress. The architecture with higher resistance was a glass-glass module with a polyolefin (POE) encapsulant, while the architecture with lower resistance was a glass-backsheet module with an ethylene vinyl acetate (EVA) encapsulant and a backsheet consisting only of Tedlar. In the former architecture, moisture ingress can only occur through the sides, while in the latter, the entire backside is available for this.

The solubility and diffusivity coefficients of all materials were assumed to have an Arrhenius dependency on temperature:

$$X = X_0\cdot e^{\left(\frac{-E_X}{RT}\right)}$$

where X_0 is the pre-exponential factor, E_X is the activation energy, R is the universal gas constant, and T is temperature. The relevant material parameters, obtained from the materials library in [63], are given in Table 2.

Dimensions of the computational domain (Fig. 3) were based on those of typical commercial crystalline silicone (c-Si) modules. Due to symmetry considerations, the domain is only a quarter of a full module. The glass and PV cells were assumed to be impermeable to moisture and were thus excluded from the diffusion domain. The time step size in the simulation was between 500 and 1000 seconds and depended on the rate of change of the moisture concentration between consecutive time stamps, with a lower rate leading to larger time steps. Since the input data were at hourly resolution, linear interpolation was used to obtain values at the required time intervals. The final finite element model consisted of 42480 elements, which provided sufficient spatial resolution to capture moisture concentration gradients while keeping computation times within practical limits.

To model ingress throughout a module's expected lifetime, the acquired time series from Section 2.2 were repeated until they spanned exactly 25 years. The model's final output was the absolute moisture concentration as a function of time at the midpoint of the encapsulant layer directly above the geometric centre of a cell located near the middle of the module. This location is indicated with an A in Fig. 3(a). For the glass-backsheet module, the moisture concentration in this location will be roughly similar to the same location above other cells, because the dominant diffusion direction is through the backsheet. For the glass-glass module, where diffusion only occurs from the sides, the concentration in location A will typically be lower than that above cells closer to the module edges.

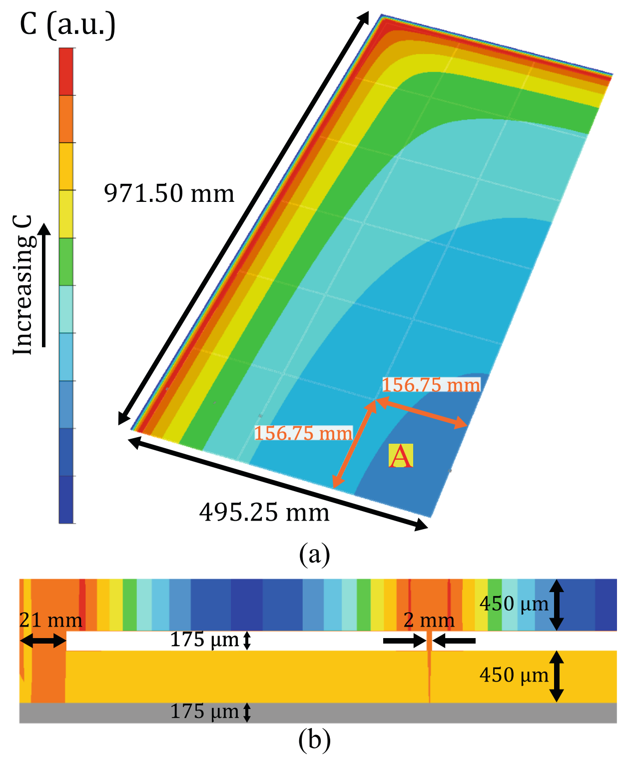

Fig. 3. Computational domain of the moisture ingress model, showing relevant dimensions and the location (A) where moisture concentration was analysed. (a): Top view of a glass-glass module with POE encapsulant. (b): Side view of the first 1.5 cells from the edge of a glass-backsheet module with EVA encapsulant and Tedlar backsheet (not to scale). The backsheet is indicated in grey. Since the modules in (a) and (b) consist of different materials, identical colours in (a) and (b) do not necessarily indicate the same moisture concentrations. Thus, the colour bar serves here only as a visual guide to indicate how moisture concentration can vary within the module.

Table 2
Solubility and diffusivity coefficients of materials used in the moisture ingress model

Material	E_D (kJ/mol)	D_0 (cm^2/s)	E_S (kJ/mol)	S_0 (g/cm^3/Pa)
EVA	38.14	2.31	16.73	1.79×10^{-5}
POE	28.19	0.26	39.49	3.79×10^{-3}
Tedlar	58.72	113.53	11.77	9.67×10^{-6}

2.4. *Lake heat flux analysis*

To assess the effect of module height over water on the on-site measurements, the Lake Heat Flux Analyzer [64] is employed, which simulates dynamic heat and water exchanges between a water body and the atmosphere. Using measurements of air temperature, RH, and wind speed at their respective heights, along with surface water temperature (all at the same timestamp) and lake altitude and latitude, the Lake Heat Flux Analyzer calculates vertical stability profiles of these variables above the water. This calculation step is done through an iterative routine (20 iterations) for turbulent flux calculations following [65]. Examples of estimated vertical profiles are shown in Fig. 4. As can be seen, the air temperature converges towards the water temperature as the height above water decreases. At the same time, the relative humidity increases towards to 100%, which is the value right at the water surface, while the wind speed decreases, which is in line with Eq. (3). From this, vertical profiles of the module temperature and RH can then be calculated for a time series using the procedure described in Section 2.2.

Since the Lake Heat Flux Analyzer requires the input of the surface water temperature and was developed for heat fluxes for ice-free lakes, vertical profiles of the stressors can only be calculated when the water body is not frozen. When lakes have a frozen surface, additional heat fluxes for melting and freezing need to be considered. In our dataset, most lakes freeze during winter. To have a year-round comparison of humidity-induced stress at different heights above the water, the Lake

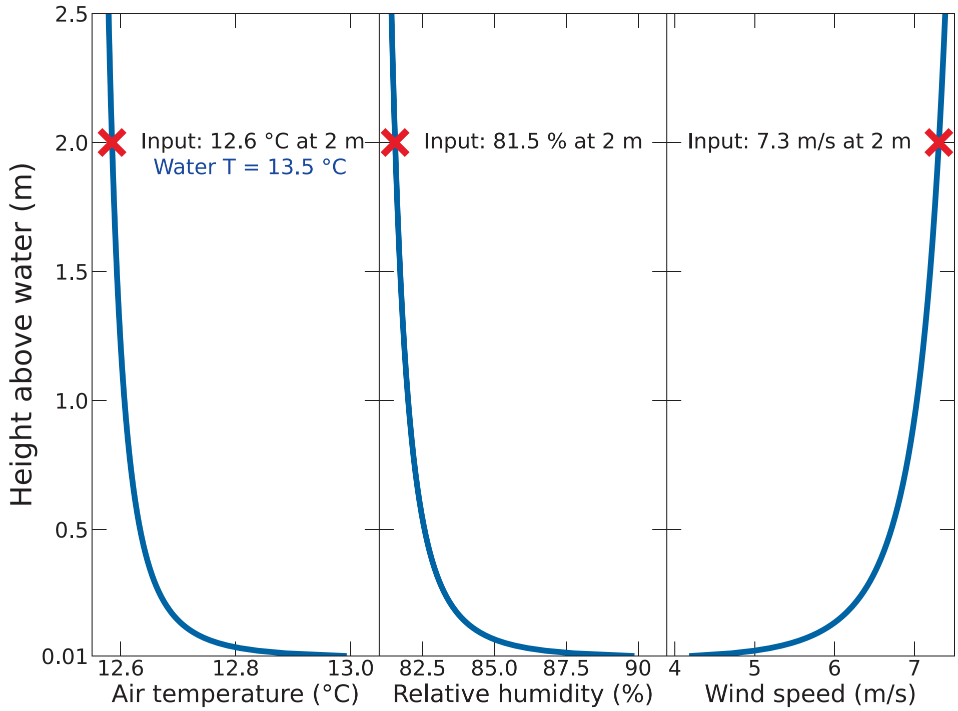

Fig. 4. Example of vertical profiles (blue lines) of air temperature, RH and wind speed above a water body at the same timestamp as calculated by the Lake Heat Flux Analyzer. Red crosses indicate measured air temperature, RH and wind speed at their given heights used as inputs to the Lake Heat Flux Analyzer. Additional inputs are the surface water temperature (indicated in blue in the left subfigure) and lake altitude and latitude. Profiles are calculated down to 1 cm above the water surface. The water surface (height = 0) forms the boundary condition, and here the air temperature becomes equal to the surface water temperature, the RH becomes equal to 100% and the wind speed becomes equal to 0 m/s.

Heat Flux Analyzer was therefore applied to only one site, TAU (TAU_S), which did not freeze.

To assess the maximum effect of changing the module height above water on humidity-induced stress, the on-site measured parameters at the instrumentation height of TAU_S (2 m) were compared with those at 1 cm above water, as derived by the Lake Heat Flux Analyzer. For this calculation, it was assumed that the environmental variables at 1 cm above water were uniform around the entire module. In reality, different parts of the module are at different heights over the water due to the module tilt, which can lead to variations in environmental conditions that are not accounted for here.

The Lake Heat Flux Analyzer calculation of the parameters at 1 cm requires surface water temperatures as one of its inputs. These were not present on TAU, as instead water temperatures were measured at 1 and 5 m depths. It was found that the temperature difference between these two depths was minimal, with absolute differences of under 1 °C for 98% of the times for which both were measured. This is due to TAU being a deep lake (mean depth 92 m) with a deep mixed layer (typically 20 m or more). The on-site measured parameters at 1 cm as calculated by the Lake Heat Flux Analyzer also showed minimal differences depending on what water temperature was used, with absolute air temperature differences of under 1°C for 99.8% of times where measurements at both depths were present, absolute RH differences of under 1 percentage point for 99.99% of datapoints, and absolute wind speed differences of under 0.1 m/s for 100% of times. As there were much more missing data at 1 m depth than at 5 m, the 5 m water temperature measurements were therefore used as the surface water temperature.

3. Results and Discussion

3.1. Ambient environment

To help understand how humidity-induced stress and degradation differ between FPV and GPV systems, the ambient stressors over water and land are compared first. Fig. 5 shows distributions of the air temperature (a), RH (b), and wind speed (c) over water (filled plots) and land (open plots) for the entire time series at hourly resolution utilizing violin- and boxplots. In addition, the distributions of absolute differences between water and land values are plotted for air temperature (d), RH (e), and wind speed (f).

The air temperature is relatively low on all sites, with mean values between 0 and 14 °C. This can be explained by the climate zones represented in our dataset, which are polar, continental, and temperate (Table 1), being relatively cold. The distribution of air temperature values is similar over water and land on all sites (Fig. 5(a)), with most of the distributions of the water-land differences centred close to 0 °C (Fig. 5(d)). The mean water-land difference in air temperature for the respective sites is between -0.5 and 1.9 °C.

The RHs are distributed around relatively high values (means between 72 and 87%; Fig. 5(b)). While for some sites, the RH distributions over water and land are similar, others show differences not centred around 0, with absolute mean differences of up to 9.0 percentage points (Fig. 5(e)). Notably, the differences in RH are in either direction, with some sites showing higher humidity levels over water than over land, while the opposite is the case for other sites. This indicates that the common assumption of increased humidity levels over water compared to over land is not generally true.

The absolute wind speed is generally higher over water than over land (Fig. 5(c) and (f)). This is in line with the reported expectation that wind speeds will be higher over open areas with lower surface roughness such as water bodies [15,56], while larger diurnal thermal fluctuations over land can promote circulations that advect air from water bodies [66]. The wind speed and direction can possibly affect RH differences between water and land, for example by land sites downwind of the lake potentially experiencing elevated RH levels. Due to the diverse distances and topologies between the respective water and land sites in this study, investigation of such effects is complicated and was beyond the focus of this study. The only case that could easily be compared were the two

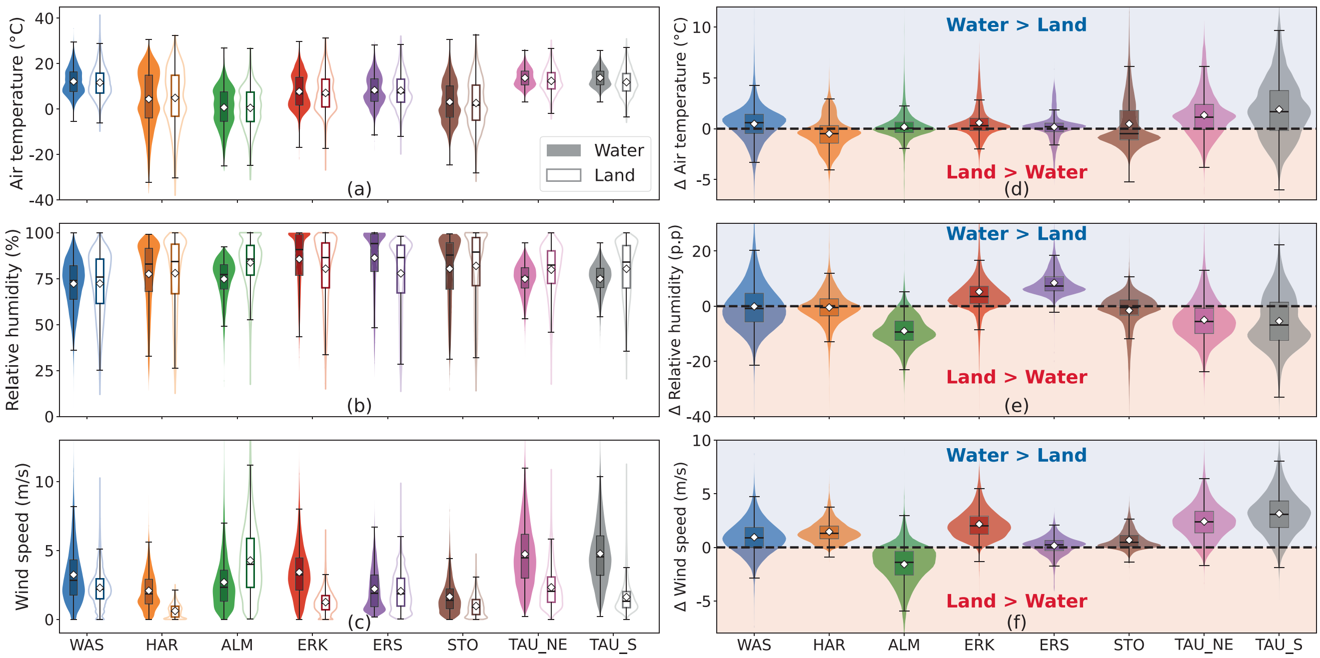

Fig. 5. Distributions of air temperature (a, d), RH (b, e) and wind speed (c, f). Subfigures a-c show absolute values over water (filled) and land (open) for all sites. Subfigures d-f display absolute differences calculated by subtracting land values from water values at all timestamps throughout the time series. The distributions are given by violin plots with boxplots inside them. The white diamonds indicate the means. Sites are given unique colours to distinguish between them more easily. This colour coding is preserved in the other figures in the results section.

land stations around TAU. Here air temperature and RH distributions were similar, despite the relatively large distance between the sites, and even though the North-Eastern station experiences higher wind speeds than the Southern one.

With the air temperatures over water and land being similar, higher wind speeds over water could possibly lead to lower module temperatures for FPV compared to GPV. As mentioned before, stressors at the module rather than in the ambient air determine moisture ingress and module degradation. The module temperature and module RH over water and land are therefore the focus in the next section.

3.2. Module environment

In Fig. 6, the absolute values and water-land differences of the modelled module temperature (a, c) and module RH (b, d) are plotted in the same way as was done for the measured ambient parameters in Fig. 5.

For each site, the distributions of module temperatures and water-land differences (Fig. 6(a) and (c)) are similar to those of the air temperatures. Exceptions are datapoints that correspond to high irradiance conditions, which cause a larger upward tail in module temperature, reaching up to 60 °C for most sites. The highest water-land module temperature differences, which are larger than the corresponding air temperature differences, also occur during these conditions. Mean water-land differences in module temperature are between -1.6 and 1.1 °C.

Just like the air and module temperatures, air and module RHs are relatively similar. Due to the mean module temperatures being higher than air temperatures, mean module RHs are slightly lower than the mean air RHs (Eq. (2), with values between 63 and 77%. Water-land differences in module RH are still in either direction for the different sites, with mean differences between -7.5 and 5.4 percentage points.

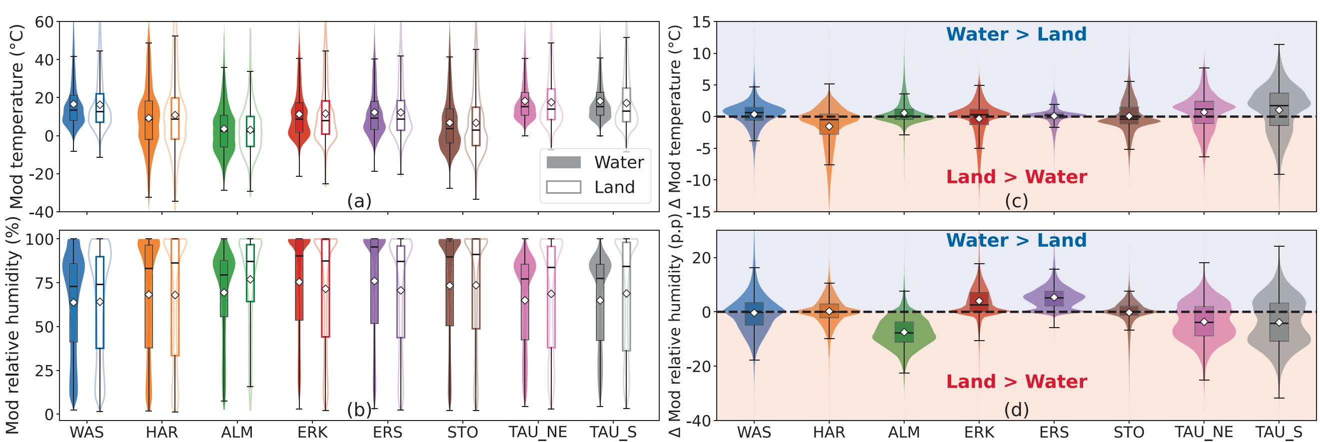

Fig. 6. Distributions of module temperature (a, c) and module RH (b, d). Subfigures a-b show absolute values over water (filled) and land (outlined) for all sites. Subfigures c-d display absolute differences calculated by subtracting land values from water values at the corresponding timestamps throughout the time series. The distributions are given by violin plots with boxplots inside them. The white diamonds indicate the means.

This confirms that humidity levels are not necessarily increased at FPV modules compared to GPV ones. For TAU, the two land stations once again have similar distributions and minimal differences in mean parameters.

With the module temperature being similar over water compared to land and with the RH being higher in either direction, humidity-induced stress and degradation are not expected to be consistently higher for FPV modules than for GPV ones. However, the module temperature and RH will differ between day and night, and it is hypothesized that these diurnal changes might be different over water compared to over land. To get a better insight into this, Fig. 7 shows the distributions of Fig. 6 split into distributions during the day (hours 6–18 in local time) and night (hours 18–6 in local time).

For both module temperature and RH, significant diurnal fluctuations are found. As expected, the module temperature is higher during the day than during the night for all sites (Fig. 7(a)), while the module RH is higher during the night (Fig. 7(b)). For almost all sites, day-night fluctuations in both module temperature and RH are larger over land than over water. Smaller day-night fluctuations in air temperature (and thus module temperature) over water reflect the higher heat capacity and heat storage of water, reducing diurnal temperature variations in the air above it. Lower module temperature fluctuations can decrease thermomechanical-related degradation and failure rates, such as solder bond failure [67]. As RH increases with decreasing temperature, the module RH shows less diurnal variation over water than over land as well.

A similar exercise to the diurnal fluctuations was performed to inspect differences between summer and winter (Fig. S1). Although a clear seasonality was seen on all sites, with higher module temperatures and lower module RHs in summer than winter, no clear seasonal trends were observed in the differences in module temperature and humidity between water and land.

In summary, the land-water stressor differences uncovered by inspection of the timeseries of ambient and module temperature and RH are modest and site dependent. However, module stress in the form of moisture ingress and related degradation have a simultaneous dependence on both temperature and humidity, making it hard to intuitively assess what the observed differences mean for degradation. To understand how the module stressors translate to internal moisture concentrations, the moisture ingress modelling results are therefore examined.

3.3. Moisture ingress modelling

The sites on which moisture ingress modelling was performed for water and land were HAR, ERK, TAU_S, and TAU_NE. These sites were selected as they displayed some of the largest water-land differences in module temperature and RH (Fig. 6(c) and (d)).

The modelled moisture content in location A (see Fig. 3) as a function of time is shown separately for the glass-backsheet (Fig. 8(a)) and the glass-glass architecture (Fig. 8(b)). As expected, the absolute concentration at location A is always lower for the glass-glass than the glass-backsheet architecture. In the glass-backsheet architecture, moisture concentration reaches an equilibrium value within 5 years. Inspection of the moisture concentration together with module temperature and RH as a function of time reveals that after equilibrium, the moisture concentration decreases in summer and increases in winter. This is caused by higher temperatures and lower RHs in summer, causing moisture to diffuse out of the module, while the lower temperatures and higher RHs in winter cause moisture to diffuse in again. Similar, although smaller fluctuations are seen at the diurnal level, with higher temperatures during the day leading to faster ingress/egress than during the night. As expected from their similar module temperature and RH distributions, the ingress curves of the two TAU land stations are similar too.

For the glass-glass architecture, concentrations have not yet reached equilibrium conditions after 25 years. Small seasonal fluctuations exist here too, with faster ingress during summer than during winter. Once again, the two TAU land stations give similar results.

To better investigate the differences in moisture ingress between water and land, the mean moisture concentration of the entire period is given in Table 3 for the investigated locations. In all but one case, the mean moisture concentration is higher over land than over water, with differences of up to 37.2%, showing that humidity-induced stress can be worse for GPV than FPV modules. Interestingly, the module architecture has a considerable effect on the water-land differences. In all locations, the water-land difference is skewed more towards land for the glass-glass compared to the glass-backsheet architecture.

To contrast the ingress in these temperate and continental climate zones with that in a tropical climate zone, moisture ingress was also modelled for a GPV module in Bangkok (hereafter referred to as BAN), with the mean concentration given in Table 3. Modelling was based on time series of module temperature and RH for BAN, which were calculated using the typical meteorological year (TMY) of the period 2005–2020 from PVGIS version 5.2 using the ERA5 solar radiation database [54]. To determine module temperature and RH from this, the same method as described in Sections 2.1 and 2.2 was applied, with some slight adaptations. Firstly, as the GHI, DNI, and DHI were included in the TMY, they did not need to be calculated. Secondly, as the albedo could not be calculated from the TMY data, it was assumed to always be

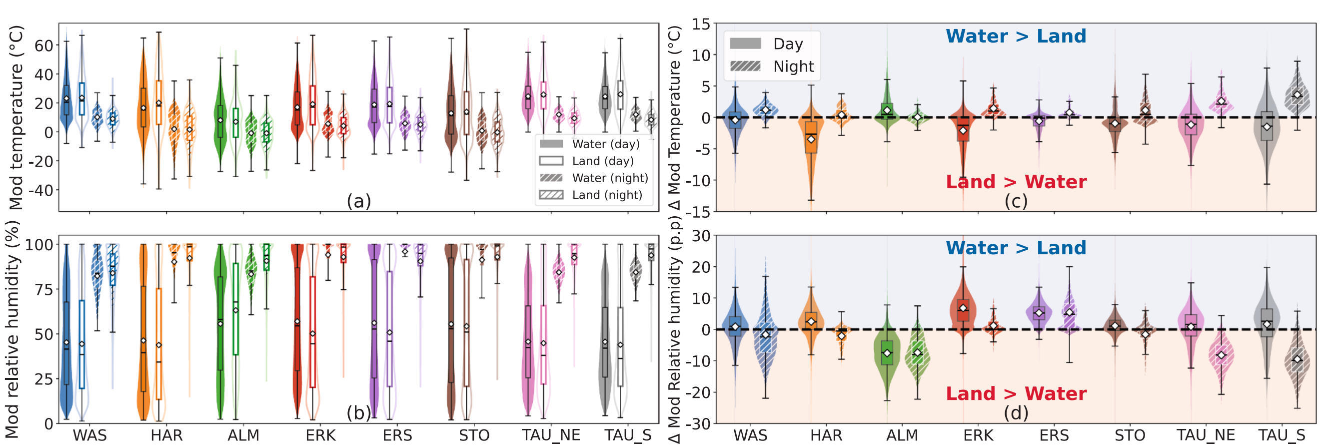

Fig. 7. Distributions of module temperature (a, c) and module RH (b, d), split in distributions during the day (filled or outlined) and night (hatched). Distributions during the day contain hours 6–18 and night contain hours 18–6 in local time. Subfigures a-b show absolute values over water (filled) and land (outlined) for all sites during the day and night. Subfigures c-d display absolute differences during the day (filled) and night (hatched) calculated by subtracting land values from water values at the corresponding timestamps throughout the time series. The distributions are given by violin plots with boxplots inside them. The white diamonds indicate the means.

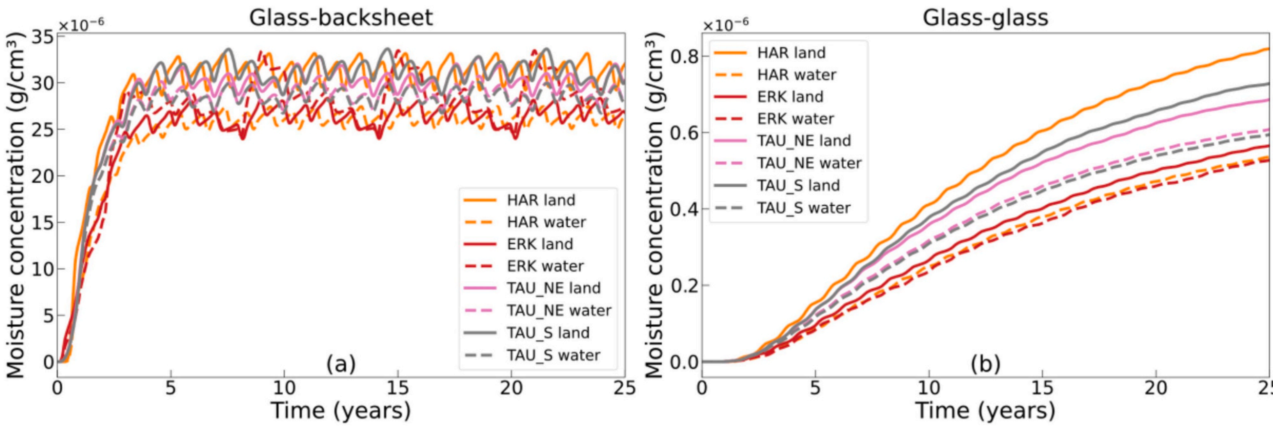

Fig. 8. Modelled moisture concentration as a function of time for selected sites. Modelled module architectures are a glass-backsheet module with EVA encapsulant and Tedlar backsheet (a) and a glass-glass module with POE encapsulant (b). As indicated by the 'A' in Fig. 3, the moisture concentration is modelled in the midpoint of the encapsulant above the centre of a cell towards the middle of the module. Locations on land have solid lines and locations over water have dashed lines.

Table 3
Mean moisture concentration throughout 25 years of exposure for different locations over water and land, and the difference therein. A positive difference means that the mean concentration over water is higher than over land.

Module architecture	Location	Case	Mean C ($\times 10^{-5}$ g/cm^3)	Water – land difference (%)
Glass-backsheet	HAR	Water	2.44	-17.2
		Land	2.94	
	ERK	Water	2.64	6.5
		Land	2.48	
	TAU_NE	Water	2.70	-5.5
		Land	2.85	
	TAU_S	Water	2.67	-8.4
		Land	2.92	
	BAN	Land	8.37	-
Glass-glass	HAR	Water	2.89×10^{-2}	-37.2
		Land	4.60×10^{-2}	
	ERK	Water	2.82×10^{-2}	-8.8
		Land	3.09×10^{-2}	
	TAU_NE	Water	3.49×10^{-2}	-11.6
		Land	3.94×10^{-2}	
	TAU_S	Water	3.40×10^{-2}	-18.0
		Land	4.14×10^{-2}	
	BAN	Land	2.45×10^{-1}	-

equal to the default value in the irradiance transposition model (0.25). BAN had a higher mean module temperature (32 °C) than the other sites, while the mean module RH of 64% was on the low end of the sites.

For both module architectures, the mean concentration for BAN is much higher than in any of the other sites (Table 3): for glass-backsheet, the concentration is 2.9–3.4 times higher, while for glass-glass, it is 5.3–8.7 times higher. This is explained by the higher module temperature in tropical climates. The glass-backsheet differences between tropical and moderate climates align with those found in other modelling studies [42], although exact differences depend highly on the temperature dependence of the diffusivity and solubility of the modelled module materials. This analysis demonstrates how differences in moisture ingress between FPV and GPV modules in the same climate zone can be much lower than between GPV modules in different climate zones. This suggests that when designing and/or testing modules for humidity-induced stress, the climate zone of deployment should be of greater concern than deployment on land or over water.

3.4. Effects of FPV system design

(i) Module height over water

So far, the analysis has assumed that the module height above water or land is equal to that of the instrumentation on the respective sites, which ranges between 1.2 and 3 meters above the surface (Table 1). However, the module height above water can vary significantly depending on the FPV system design. As mentioned in Section 2.4, to assess the maximum effect of changing the module height above water on humidity-induced stress, the on-site measured parameters at the instrumentation height (2 m) were compared with those at 1 cm above water, as derived by the Lake Heat Flux Analyzer for TAU.

Distributions of the on-site measured parameters for TAU at 2 m and 1 cm over water and their absolute differences are shown in Fig. 9 in the same style as Figs. 5 and 6. The air temperature (Fig. 9(a) and (d)) generally increases when getting closer to the lake surface, although there are occurrences of decreasing temperatures. This is explained by the fact that for this site, the water temperature was higher than the air temperature for 80% of the time series. Lower water than air water temperatures occur mostly during spring, when the air temperatures increase faster than the water temperatures. For other water bodies where water temperatures do not exceed air temperatures as often, more instances of decreasing air temperature when getting closer to the water surface can be expected. The RH (Fig. 9(b) and (e)) always increases when going from 2 m to 1 cm above the lake surface, while the wind speed always decreases (Fig. 9(c) and (f)).

Following the changes in on-site measured parameters when getting closer to the water surface (Fig. 9), both the module temperature and RH generally increase as well (Fig. 10). The mean module temperature is 1.3 °C higher at 1 cm than at 2 m, while the mean module RH is 8.6 percentage points higher. These numbers are similar to the highest reported water-land differences (Section 3.2). This indicates that a change in the module height over water can have a similar, if not greater, effect on these module stressors compared to the effect of installing modules over water instead of on land. It should be noted that the gradient in stressor level is typically highest close to the water surface (Fig. 4). Stressor differences will thus be smaller when compared at different heights further above the water. This also means that as all sensors are relatively high above water and land (Table 1), the difference in sensor height for measurements of the same type between water and land are expected to have a minimal effect on the measurements.

To assess the effect of the difference in module temperature and RH on humidity-induced stress, moisture ingress modelling was performed for the 1 cm case as well and compared to the 2 m case that was presented in Section 3.3. In a similar fashion to Fig. 8, modelled moisture concentrations for the glass-backsheet and glass-glass architectures are shown in Fig. 11. Due to the increased module temperature and RH at 1 cm compared to 2 m, internal moisture concentrations are higher as well. For the glass-backsheet architecture, the mean concentration is

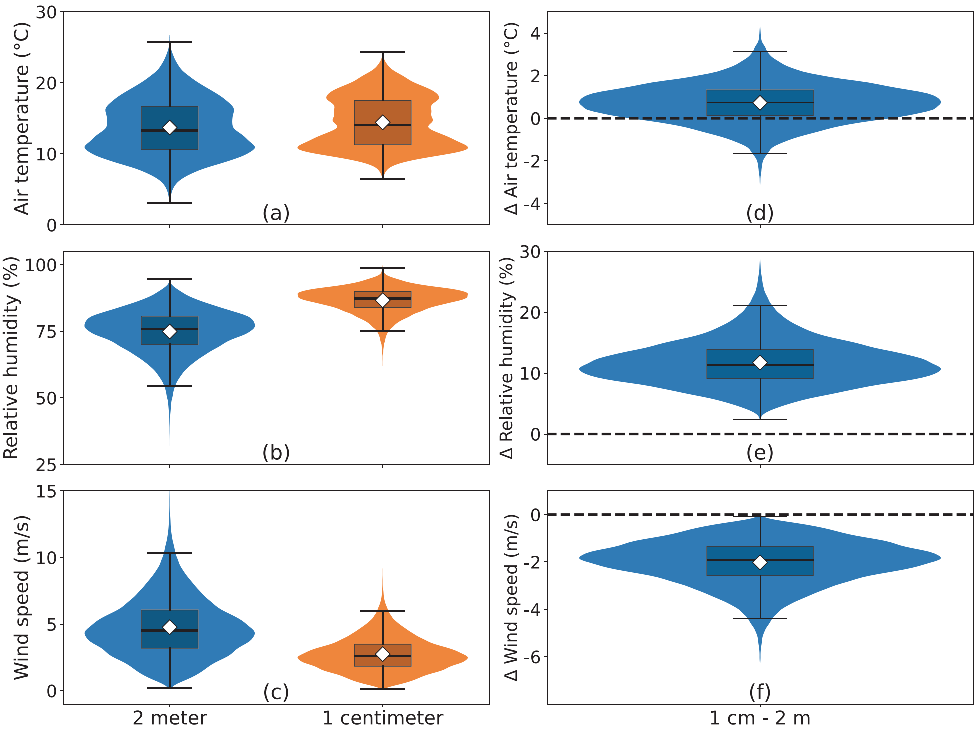

Fig. 9. Distributions of air temperature (a, d), RH (b, e) and wind speed (c, f) measurements at hourly resolution for TAU at 2 m and 1 cm above the water surface. Subfigures a-c show absolute values over water at both heights. Subfigures d-f display absolute differences calculated by subtracting the values at 2 m from values at 1 cm throughout the time series. The distributions are given by violin plots with boxplots inside them. The white diamonds indicate the means.

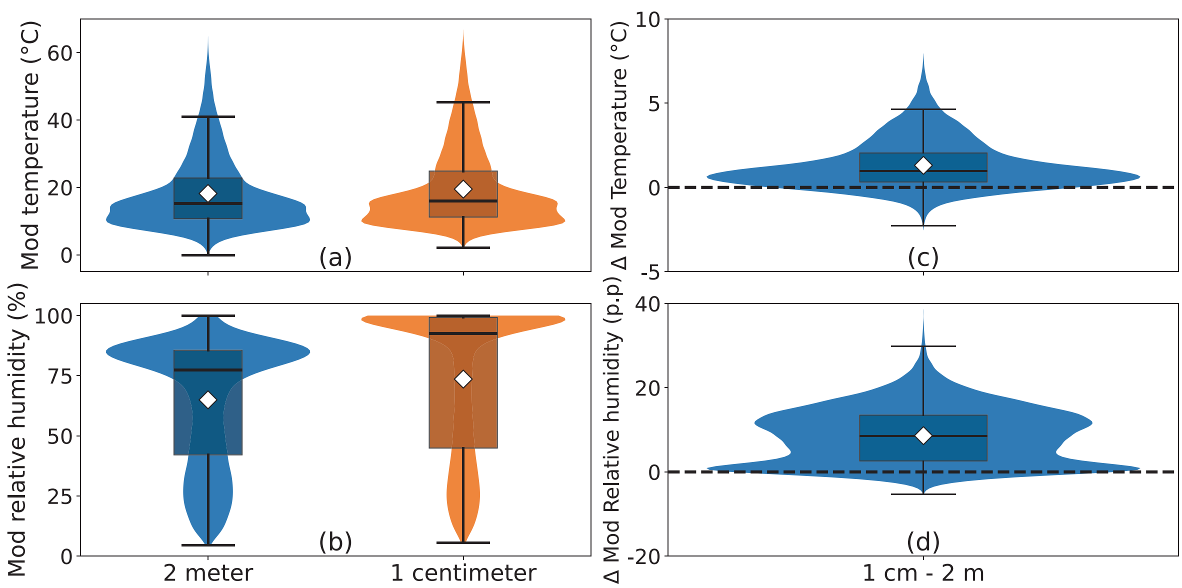

Fig. 10. Distributions of module temperature (a, c) and module RH (b, d) at hourly resolution for TAU at 2 m and 1 cm above the water surface. Subfigures a-c show absolute values over water at both heights. Subfigures d-f display absolute differences calculated by subtracting the values at 2 m from values at 1 cm throughout the time series. The distributions are given by violin plots with boxplots inside them. The white diamonds indicate the means.

29.7% higher, while for the glass-glass architecture, it is 47.0%. This is larger than the water-land differences at the respective sites (Table 3), further confirming that the module height over water can have a larger impact on humidity-induced stress than whether the module is installed over water or on land.

(ii) Enhanced module cooling

As mentioned in Section 2.1, this section illustrates the effect of higher U-values on FPV module temperature and RH by re-evaluating these variables under elevated U-values of 45 W/m^{2}C for u_0 and 10 W/m^{2}C·m/s for u_1, opposed to the default values 20.74 W/m^{2}C for u_0 and 2.91 W/m^{2}C·m/s for u_1 used so far.

Fig. 12 shows the distributions of module temperature (a) and RH (b) over water with default (filled) and increased (open) U-values, and the absolute differences between the two (c, d). As expected, for all sites the module temperature is generally lower for increased U-values (Fig. 12 (a) and (c)), with absolute mean differences between default and

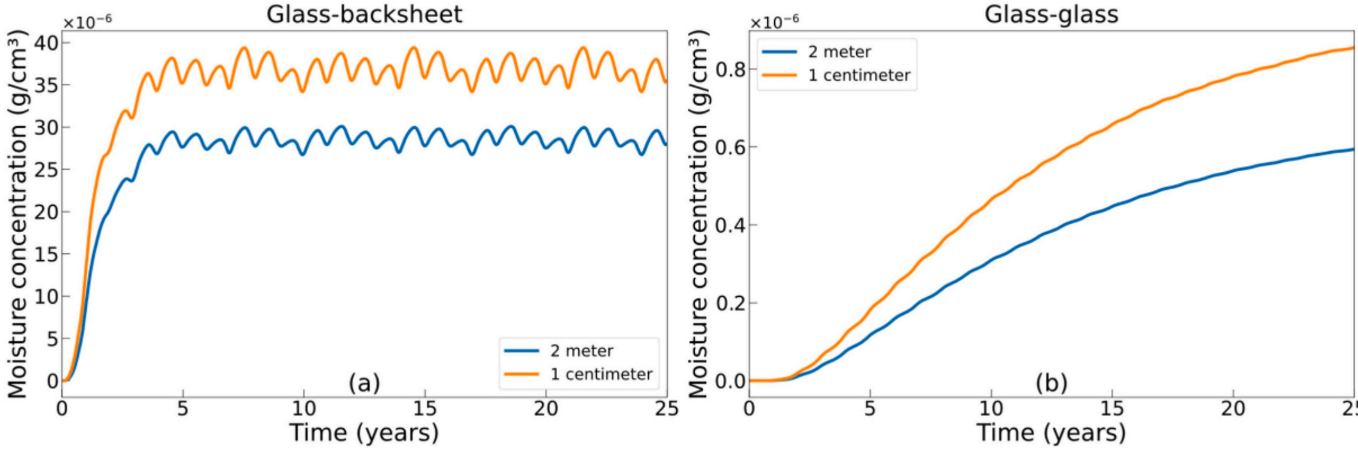

Fig. 11. Modelled moisture concentration as a function of time for TAU_S at a module height of 2 meters or 1 centimeter over water. Modelled module architectures are a glass-backsheet module with EVA encapsulant and Tedlar backsheet (a) and a glass-glass module with POE encapsulant (b). As indicated by the 'A' in Fig. 3, the moisture concentration is modelled in the midpoint of the encapsulant above the centre of a cell towards the middle of the module.

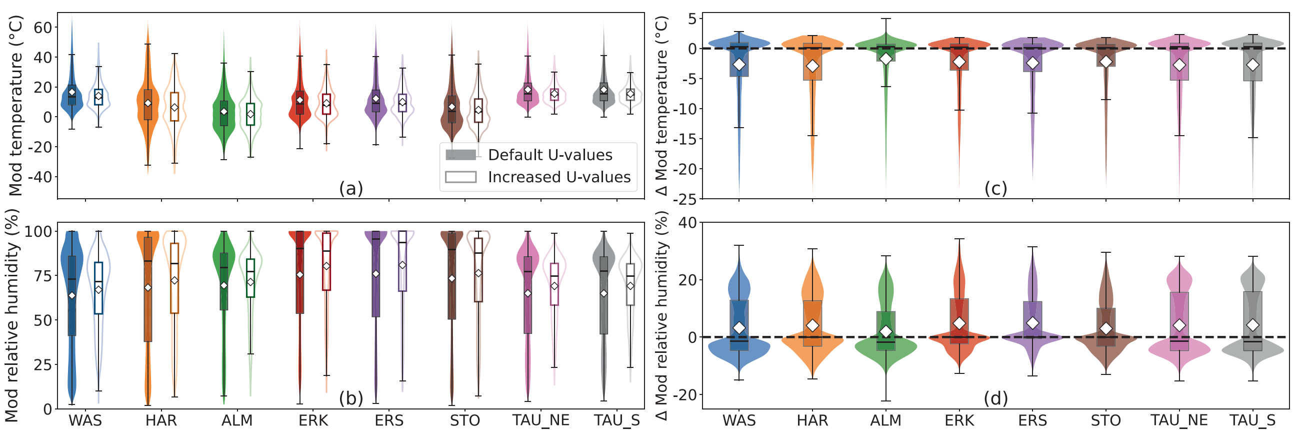

Fig. 12. Distributions of module temperature (a, c) and module RH (b, d) over water. Subfigures a-b show absolute values over water calculated with default (filled) and increased (outlined) U-values. Subfigures c-d display absolute differences calculated by subtracting the parameters with default U-values values from those with increased U-values at the corresponding timestamps throughout the time series. The distributions are given by violin plots with boxplots inside them. The white diamonds indicate the means.

increased U-values being up to 3 °C. This is far greater than the mean module temperature differences between water and land (Fig. 6). Due to the decrease in module temperature, module RHs are generally higher for increased U-values compared to default values (Fig. 12(b) and (d)), with mean differences of up to 4.9 percentage points. While substantial, this is lower than the mean module RH differences between water and land (Fig. 6).

The distributions of the differences (Fig. 12(c) and (d)) show a broad area with small differences for both variables. These are positive for the module temperature and negative for the module RH. This area is combined with a narrower tail of larger differences in the opposite direction. Inspection of Eq. (1) shows that the small positive module temperature differences occur when the ambient temperature exceeds the module temperature, which is during low irradiance conditions. As the fraction in Eq. (1) is negative during these times, an increase in U-values leads to a higher module temperature. As mentioned previously, the increase in module temperature causes a decrease in module RH (Fig. 12(d)). The tails of larger negative module temperature and positive module RH differences occur during high irradiance conditions when the module temperature exceeds the air temperature, which is when an increase in U-values causes a decrease in module temperature. By increasing module temperatures during low irradiance conditions and decreasing them during high irradiance conditions, an increase in U-values thus decreases diurnal module temperature and RH fluctuations.

As most of the data in the respective time series are at low irradiances, there are more occurrences of small module temperature and RH differences than large ones, causing relatively modest mean module temperature and RH differences between default and increased U-values. For locations with a larger fraction of higher irradiances, mean differences are therefore expected to be larger.

Once again, to quantify the effect of higher U-values on humidity-induced stress, moisture ingress was modelled for higher U-values and compared to the default ones for the sites selected in Section 3.4 (Fig. 13). As TAU_S water and TAU_NE water are essentially identical (same measurements, but different removal and filling of data dependent on the respective land stations), only TAU_S water was included in this analysis. Fig. 13 shows that for all three modelled locations, ingress is higher for the default U-values than for the increased ones, indicating that the decrease in module temperature has a higher effect on ingress than the increase in module RH. Furthermore, seasonal concentration fluctuations are higher for the default compared to the increased U-values. Differences in mean concentration between default and higher U-values are between 20.7 and 24.5% for the glass-backsheet architecture, and between 38.0 and 42.0% for glass-glass. These are once again larger than the differences between water and land (Table 3). This indicates how, similar to module height over water, the operating module

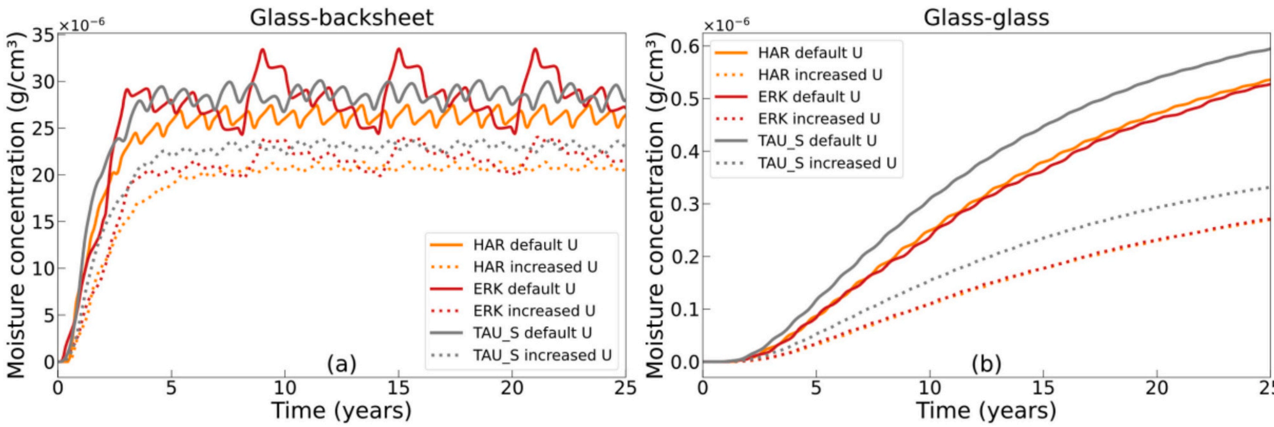

Fig. 13. Modelled moisture concentration as a function of time for selected locations over water using default (solid lines) or increased U-values (dotted lines). Modelled module architectures are a glass-backsheet module with EVA encapsulant and Tedlar backsheet (a) and a glass-glass module with POE encapsulant (b). As indicated by the 'A' in Fig. 3, the moisture concentration is modelled in the midpoint of the encapsulant above the centre of a cell towards the middle of the module.

temperature can have a larger effect on moisture ingress than whether the module is installed on land or over water.

3.5. Implications and limitations of study

Several aspects of the study's scope affect the obtained results. Most importantly, no PV systems were present on any of the sites. As a result, discrepancies might be expected between modelled and real-world module stressors, as the physical presence of PV modules might affect the ambient parameters. Modules can act as wind barriers [68], likely leading to temperature variations within a single system due to differences in wind speed [69]. Moreover, the presence of FPV systems can influence the RH in the air. Especially for FPV systems with closely-packed modules that are mounted close to the water surface without intermediary buoyant structures, there is a chance of high humidity levels directly underneath the modules as evaporation is obstructed. This effect is especially important for the vertical translation of the on-site measured parameters. Furthermore, to ensure a consistent comparison between FPV and GPV, module tilt angles were identical and optimized for maximum annual energy production at each location. In reality, FPV modules are typically installed at reduced tilt angles to minimize wind-induced uplift and drift forces [70]. A lower than optimal tilt angle generally decreases the plane of array irradiance and with it the module temperature, thereby increasing module RH. To quantify the impacts of these assumptions, comparisons of modelled module temperatures and RHs with measurements around real FPV and GPV systems are recommended.

Beyond the effect of the physical presence of the PV system on module stressors, the module material properties will significantly affect moisture ingress. While the ingress modelling was based on material parameters from a standardized library, it is important to recognize that common module material types, such as EVA and POE, can span a wide range of different products with varying solubility and diffusivity coefficients [63]. Therefore, the specific material selection used in modelling can significantly alter simulated moisture concentrations.

This study focused specifically on water vapor effects, but liquid water can affect module degradation too. The presence of liquid water in or on modules is for example reported to accelerate delamination [71], potential induced degradation (PID) [35] and corrosion [72]. FPV modules may thus experience additional water-induced stress and degradation that is not considered here.

Lastly, while the study included diverse sites with varying characteristics such as lake size, all sites were present in relatively cold climates. Similar analyses in warmer climates could possibly reveal larger differences between water and land, as well as a larger impact of increased U-values, and are therefore recommended.

4. Summary and conclusion

This study has aimed to help fill the research gap on humidity-induced stress in FPV modules and how this compares to GPV. This was done by comparing multi-year meteorological datasets over seven inland water bodies located in relatively cold climates with those over nearby land locations. While ambient and calculated module temperatures were comparable above water and land (mean differences of maximum 1.6 °C), larger RH differences were found (mean differences of up to 7.5 percentage points), with some sites showing higher values over land, and others over water. This challenges the common assumption of universally higher humidity levels for FPV modules compared to GPV ones, and rather shows that site to site differences can have a larger impact on these stressors than being on water or land. Diurnal fluctuations in both module temperature and RH were stronger over land, attributed to the stabilizing influence of water.

To quantify the impact of these differences on humidity-induced stress, moisture ingress was modelled towards the centre of two different module architectures for the sites with the largest water-land differences. Modelled internal moisture concentrations were generally lower over water (mean differences of up to 37%). However, these water-land differences were much smaller than those observed on land between cold climates and a tropical one (up to 8 times higher mean moisture concentration). This suggests that the climate zone of deployment, rather than installation over water or on land, should be the primary consideration for module design and testing related to humidity-induced degradation.

Lastly, analysis of FPV system design parameters, specifically the module height above water and enhanced module cooling, revealed a substantial impact on humidity-induced stress. Both reduced module height and increased cooling led to changes in modelled moisture concentrations that exceeded the observed water-land differences (up to 47% and 42% higher mean moisture concentration, respectively). This indicates that FPV system design can have a larger influence on humidity-induced stress than the choice of FPV versus GPV.

By providing these nuances, the present work advances the understanding of humidity-induced stress for FPV, and thereby in more general that of FPV module reliability. However, it is limited by the absence of operational PV systems and sites in warmer climates. To corroborate and extend our findings, measurements on real FPV systems are recommended, particularly in warmer climates where water-land differences might be more pronounced.

CRediT authorship contribution statement

Nathan Roosloot: Writing – review & editing, Writing – original draft, Visualization, Methodology, Investigation, Formal analysis, Data curation. **Dag Lindholm:** Writing – review & editing, Methodology, Formal analysis. **Sayan Adhikari:** Writing – review & editing, Formal analysis. **François Clayer:** Writing – review & editing, Methodology, Investigation, Formal analysis. **Curtis L. DeGasperi:** Writing – review & editing, Data curation. **Blaize A. Denfeld:** Writing – review & editing, Data curation. **Piet Verburg:** Writing – review & editing, Data curation. **Huaxia Yao:** Writing – review & editing, Data curation. **James A. Rusak:** Writing – review & editing, Data curation. **Ankur R. Desai:** Writing – review & editing, Data curation. **Daniel Hornbach:** Writing – review & editing, Data curation. **Katy Nugent:** Writing – review & editing, Data curation. **Ulrike Obertegger:** Writing – review & editing, Data curation. **Kiyoko Yokota:** Writing – review & editing, Data curation. **Junhong Wang:** Writing – review & editing, Data curation. **Torunn Kjeldstad:** Writing – review & editing, Project administration, Funding acquisition. **Josefine H. Selj:** Writing – review & editing, Supervision, Project administration, Funding acquisition. **Gaute Otnes:** Writing – review & editing, Supervision, Project administration, Methodology, Investigation, Funding acquisition, Conceptualization.

Declaration of competing interest

The authors declare that they have no known competing financial interests or personal relationships that could have appeared to influence the work reported in this paper.

Acknowledgements

This work was supported by the Norwegian Research Council through the project HydroSun (grant number 328640) and by the European Union's Horizon Europe research and innovation program through the project SuRE (grant agreement 101135567). The authors benefitted from the Global Lake Ecological Observatory Network (GLEON), through which the on-site measured data from all sites were found.

Swedish lake data (Erssjön, Erken, Stortjärn, and Almbergasjön) has been made possible by the Swedish Infrastructure for Ecosystem Science (SITES) at stations Abisko, Erken, Skogaryd, Svartberget, which is funded by the Swedish Research Council. Additional data for Abisko and Erken was provided by ICOS Carbon Portal and SMHI, respectively. Harp lake data was funded by the Ontario Ministry of the Environment, Conservation and Parks with Chris McConnell and Tim Field providing invaluable assistance with buoy data collection and maintenance. Washington Lake data was provided by King County Water and Land Resources Division. Field and laboratory support were provided by the King County Environmental Laboratory. The Lake Taupo monitoring buoy was installed by the National Institute of Water and Atmospheric Research.

ERA5 data [44] was downloaded from the Copernicus Climate Change Service (2023). The results contain modified Copernicus Climate Change Service information 2020. Neither the European Commission nor ECMWF is responsible for any use that may be made of the Copernicus information or data it contains. ARD acknowledges support from the US National Science Foundation (NSF) North Temperate Lakes Long-Term Ecological Research program, #DEB-2025982 and the UW-Madison Research Forward program.

Data availability

Timeseries of the on-site measured data, the module temperature and RH and the modelled moisture concentrations at location A, on which Figs. 5–13 are based, are openly available on [73]. For most of the Swedish lakes, links to the on-site measured data are shared rather than the data itself upon request of the data provider.

Declaration of generative AI and AI-assisted technologies in the manuscript preparation process

During the preparation of this work the authors used Open AI's GPT-4, Anthropic's Claude 3.5 Sonnet and Google's Gemini 2.5 as tools for minor text revisions and programming assistance. After using these tools, the authors reviewed and edited the content as needed and take full responsibility for the content of the publication.

Declaration of generative AI and AI-assisted technologies in the manuscript preparation process

During the preparation of this work the authors used Open AI's GPT-4, Anthropic's Claude 3.5 Sonnet and Google's Gemini 2.5 as tools for minor text revisions and programming assistance. After using these tools, the authors reviewed and edited the content as needed and take full responsibility for the content of the publication.

Appendix A. Supplementary data

Supplementary data to this article can be found online at https://doi.org/10.1016/j.solener.2026.114923.

References

[1] T. Reindl, Overview, Status and outlook of floating PV. in *4th International Integrated PV Workshop*, 2025.
[2] World Bank Group, ESMAP, and SERIS, "Where Sun Meets Water: Floating Solar Market Report,", World Bank, Washington, DC, 2019.
[3] A.E. Cagle, A. Armstrong, G. Exley, S.M. Grodsky, J. Macknick, J. Sherwin, R. R. Hernandez, The Land Sparing, Water Surface Use Efficiency, and Water Surface Transformation of Floating Photovoltaic Solar Energy Installations, Sustainability 12 (19) (2020) 8154, https://doi.org/10.3390/su12198154.
[4] S. Brown, R. J. Nicholls, C. D. Woodroffe, S. Hanson, J. Hinkel, A. S. Kebede, B. Neumann, and A. T. Vafeidis, "Sea-Level Rise Impacts and Responses: A Global Perspective," in *Coastal Hazards*, C. W. Finkl, Ed., Dordrecht: Springer Netherlands, 2013, pp. 117–149. doi: 10.1007/978-94-007-5234-4_5.
[5] B. Neumann, A.T. Vafeidis, J. Zimmermann, R.J. Nicholls, Future coastal population growth and exposure to sea-level rise and coastal flooding - a global assessment, PLoS One 10 (3) (2015) e0118571, https://doi.org/10.1371/journal.pone.0118571.
[6] International Energy Agency, "Trends In Photovoltaic Applications 2024," 2024.
[7] Y. Jin, S. Hu, A.D. Ziegler, L. Gibson, J.E. Campbell, R. Xu, D. Chen, K. Zhu, Y. Zheng, B. Ye, F. Ye, Z. Zeng, Energy production and water savings from floating solar photovoltaics on global reservoirs, Nat. Sustain. 6 (7) (2023) 865–874, https://doi.org/10.1038/s41893-023-01089-6.
[8] S. Gadzanku, H. Mirletz, N. Lee, J. Daw, A. Warren, Benefits and Critical Knowledge Gaps in Determining the Role of Floating Photovoltaics in the Energy-Water-Food Nexus, Sustainability 13 (8) (2021) 4317, https://doi.org/10.3390/su13084317.
[9] N. Lee, U. Grunwald, E. Rosenlieb, H. Mirletz, A. Aznar, R. Spencer, S. Cox, Hybrid floating solar photovoltaics-hydropower systems: Benefits and global assessment of technical potential, Renew. Energy 162 (2020) 1415–1427, https://doi.org/10.1016/j.renene.2020.08.080.
[10] R. Gonzalez Sanchez, I. Kougias, M. Moner-Girona, F. Fahl, A. Jäger-Waldau, "Assessment of floating solar photovoltaics potential in existing hydropower reservoirs in Africa, Renew. Energy 169 (2021) 687–699, https://doi.org/10.1016/j.renene.2021.01.041.
[11] O. Delbeke, J. D. Moschner, and J. Driesen, "The complementarity of offshore wind and floating photovoltaics in the Belgian North Sea, an analysis up to 2100," *Renew. Energy*, vol. 218, no. August, p. 119253, Dec. 2023, doi: 10.1016/j.renene.2023.119253.
[12] K. Ilgen, D. Schindler, A. Armbruster, R. Ladwig, I. Eppinger Ruiz de Zarate, and J. Lange, "Evaporation reduction and energy generation potential using floating photovoltaic power plants on the Aswan High Dam Reservoir," *Hydrological Sciences Journal*, vol. 69, no. 6, pp. 709–720, Apr. 2024, doi: 10.1080/02626667.2024.2332625.
[13] D. Lindholm, T. Kjeldstad, J. Selj, E.S. Marstein, H.G. Fjær, Heat loss coefficients computed for floating PV modules, Prog. Photovolt. Res. Appl. 29 (12) (2021) 1262–1273, https://doi.org/10.1002/pip.3451.
[14] L. Micheli, The temperature of floating photovoltaics: Case studies, models and recent findings, Sol. Energy 242 (2022) 234–245, https://doi.org/10.1016/j.solener.2022.06.039.
[15] IEA PVPS Task 13, "Floating Photovoltaic Power Plants: A Review of Energy Yield, Reliability, and Maintenance," 2025.
[16] International Energy Agency, "Trends In Photovoltaic Applications 2023," 2023.
[17] J. Ascencio-Vásquez, I. Kaaya, K. Brecl, K.-A. Weiss, M. Topič, Global climate data processing and mapping of degradation mechanisms and degradation rates of PV

modules, Energies (Basel) 12 (24) (2019) 4749, https://doi.org/10.3390/en12244749.
[18] M. Koehl, M. Heck, S. Wiesmeier, Categorization of weathering stresses for photovoltaic modules, Energy Sci. Eng. 6 (2) (2018) 93–111, https://doi.org/10.1002/ese3.189.
[19] G. Jorgensen, K. Terwilliger, J. DelCueto, S. Glick, M. Kempe, J. Pankow, F. Pern, T. McMahon, Moisture transport, adhesion, and corrosion protection of PV module packaging materials, Sol. Energy Mater. Sol. Cells 90 (16) (2006) 2739–2775, https://doi.org/10.1016/j.solmat.2006.04.003.
[20] L. Spinella, S. Uličná, A. Sinha, D.B. Sulas-Kern, M. Owen-Bellini, S. Johnston, L. T. Schelhas, Chemical and mechanical interfacial degradation in bifacial glass/glass and glass/transparent backsheet photovoltaic modules, Prog. Photovolt. Res. Appl. 30 (12) (2022) 1423–1432, https://doi.org/10.1002/pip.3602.
[21] G. R. Mon, "Observations of solar-cell metallization corrosion," in *Proc. of the Flat-Plate Solar Array Res. Forum on Photovoltaic Metallization Systems*, 1983, pp. 137–146.
[22] O.K. Segbefia, A.G. Imenes, T.O. Sætre, Moisture ingress in photovoltaic modules: a review, Sol. Energy 224 (2021) 889–906, https://doi.org/10.1016/j.solener.2021.06.055.
[23] M. Kontges *et al.*, "Review of failures of photovoltaic modules," 2014.
[24] M. Theristis, J.S. Stein, C. Deline, D. Jordan, C. Robinson, W. Sekulic, A. Anderberg, D.J. Colvin, J. Walters, H. Seigneur, B.H. King, Onymous early-life performance degradation analysis of recent photovoltaic module technologies, Prog. Photovolt. Res. Appl. 31 (2) (2023) 149–160, https://doi.org/10.1002/pip.3615.
[25] A. Louwen, S. Lindig, G. Chowdhury, and D. Moser, "Climate- and Technology-Dependent Performance Loss Rates in a Large Commercial Photovoltaic Monitoring Dataset," *Solar RRL*, vol. 8, no. 5, Mar. 2024, doi: 10.1002/solr.202300653.
[26] VDMA, "International Technology Roadmap for Photovoltaics (ITRPV) - 2023 Results," 2024.
[27] C. Sen, H. Wang, M. U. Khan, J. Fu, X. Wu, X. Wang, and B. Hoex, "Buyer aware: Three new failure modes in TOPCon modules absent from PERC technology," *Solar Energy Materials and Solar Cells*, vol. 272, no. March, p. 112877, Aug. 2024, doi: 10.1016/j.solmat.2024.112877.
[28] L. Pirot-Berson, R. Couderc, R. Bodeux, and J. Dupuis, "Failure modes of silicon heterojunction photovoltaic modules in damp heat environment: Sodium and moisture effects," *Solar Energy Materials and Solar Cells*, vol. 278, no. October, p. 113190, Dec. 2024, doi: 10.1016/j.solmat.2024.113190.
[29] D. C. Jordan and T. M. Barnes, "Degradation Science from Nanometers to Kilometers: A Pathway to Rapid Detection for Reliable Photovoltaics," *Solar RRL*, vol. 7, no. 17, 2023, doi: 10.1002/solr.202300170.
[30] A. M. Ajmal, Y. Yang, and Y. Zhu, "Degradation rate analysis of offshore PV module applications considering climatic stresses and salinity effects," *Solar Energy*, vol. 295, no. April, p. 113522, Jul. 2025, doi: 10.1016/j.solener.2025.113522.
[31] N. M. Naushad, G. R. Rimon, and M. R. Khan, "Local temperature and humidity aware prediction of degradation, lifetime, and long-term yield of mono- and bifacial floating photovoltaic systems," *Solar Energy*, vol. 299, no. February, p. 113639, Oct. 2025, doi: 10.1016/j.solener.2025.113639.
[32] S.Z. Golroodbari, W. van Sark, Simulation of performance differences between offshore and land-based photovoltaic systems, Prog. Photovolt. Res. Appl. 28 (9) (2020) 873–886, https://doi.org/10.1002/pip.3276.
[33] S. Kaplanis, E. Kaplani, J.K. Kaldellis, PV Temperature Prediction Incorporating the Effect of Humidity and Cooling Due to Seawater Flow and Evaporation on Modules Simulating Floating PV Conditions, Energies (Basel) 16 (12) (2023) 4756, https://doi.org/10.3390/en16124756.
[34] SERENDI-PV, "D4.1 Definition of new needs and specifications on current QC procedures and equipment," 2021.
[35] T. Reindl, C. Paton, A. Kumar, H. Liu, V. A. Krishnamurthy, C. Tan, L. Vinayagam, S. A. Ting, Z. Dobrotkova, S. Chavez, G. Gregoire, D. Harwood, J. Johnson, S. K. Ooi, and P. Y. Wong, "Where Sun Meets Water: Floating Solar Handbook for Practitioners," 2019.
[36] N. Kyranaki, A. Van Der Heide, H. J. Lomeri, I. Kaaya, S. Bouguerra, J. D. Moschner, A. Morlier, and M. Daenen, "Material Selection and Novel Reliability Testing for Floating Photovoltaic Modules," in *41st European Photovoltaic Solar Energy Conference and Exhibition*, 2024, pp. 020250-001-020250–016.
[37] Y. Li, W. Lin, W. Yang, C.-F. Hsieh, Sequential acceleration tests with pressure cooker test (PCT) and UV for backsheets of PV modules, Energy Procedia 150 (2018) 44–49, https://doi.org/10.1016/j.egypro.2018.09.009.
[38] "Examples of news articles on FPV specific modules." Accessed: Nov. 14, 2025. [Online]. Available: https://www.pv-magazine.com/2025/06/25/gcl-si-presents-solar-modules-for-offshore-projects/; https://www.jasolar.com/index.php?m=content&c=index&a=show&catid=419&id=557; https://www.pv-magazine.com/2020/11/19/hanwha-q-cells-unveils-special-floating-pv-panel.
[39] B. Amiot, M. Chiodetti, R. Le Berre, K. Radouane, D. Boublil, P. Dupeyrat, K. Vermeyen, and S. Giroux-Julien, "Floating photovoltaics - On-site measurements in temperate climate and lake influence on module behavior," in *37th European Photovoltaic Solar Energy Conference and Exhibition*, 2020, pp. 1772–1776. doi: 10.4229/EUPVSEC20202020-6DO.15.2.
[40] W. Luo, S.N. Isukapalli, L. Vinayagam, S.A. Ting, M. Pravettoni, T. Reindl, A. Kumar, Performance loss rates of floating photovoltaic installations in the tropics, Sol. Energy 219 (2021) 58–64, https://doi.org/10.1016/j.solener.2020.12.019.
[41] S. K. A. Dzamesi, W. Ahiataku-Togobo, S. Yakubu, P. Acheampong, M. Kwarteng, R. Samikannu, and E. Azeave, "Comparative performance evaluation of ground-mounted and floating solar PV systems," *Energy for Sustainable Development*, vol. 80, no. January, p. 101421, Jun. 2024, doi: 10.1016/j.esd.2024.101421.
[42] S. Mitterhofer, J. Ascencio Vásquez, and X. Gu, "Worldwide Moisture Ingress Evaluation in Photovoltaic Modules Using Finite Element Simulations and Machine Learning," in *8th World Conference on Photovoltaic Energy Conversion*, 2022, pp. 609–613. doi: 10.4229/WCPEC-82022-3EO.1.3.
[43] D.J. Coyle, Life prediction for CIGS solar modules part 1: modeling moisture ingress and degradation, Prog. Photovolt. Res. Appl. 21 (2) (2013) 156–172, https://doi.org/10.1002/pip.1172.
[44] H. Hersbach, B. Bell, P. Berrisford, G. Biavati, A. Horányi, J. Muñoz Sabater, J. Nicolas, C. Peubey, R. Radu, I. Rozum, D. Schepers, A. Simmons, C. Soci, D. Dee, and J.-N. Thépaut, "ERA5 hourly data on single levels from 1940 to present," Copernicus Climate Change Service (C3 S) Climate Data Store (CDS).
[45] A. Driesse, J. Stein, and M. Theristis, "Improving Common PV Module Temperature Models by Incorporating Radiative Losses to the Sky," Albuquerque, NM, and Livermore, CA (United States), Aug. 2022. doi: 10.2172/1884890.
[46] M. Dörenkämper, A. Wahed, A. Kumar, M. de Jong, J. Kroon, T. Reindl, The cooling effect of floating PV in two different climate zones: A comparison of field test data from the Netherlands and Singapore, Sol. Energy 214 (2021) 239–247, https://doi.org/10.1016/j.solener.2020.11.029.
[47] M. Koehl, M. Heck, S. Wiesmeier, Modelling of conditions for accelerated lifetime testing of Humidity impact on PV-modules based on monitoring of climatic data, Sol. Energy Mater. Sol. Cells 99 (2012) 282–291, https://doi.org/10.1016/j.solmat.2011.12.011.
[48] A.L. Buck, Buck research cr-1a user's manual, Appendix 1, Boulder, Colorado, 1996.
[49] I. Reda, A. Andreas, Solar position algorithm for solar radiation applications, Sol. Energy 76 (5) (2004) 577–589, https://doi.org/10.1016/j.solener.2003.12.003.
[50] K. S. Anderson, C. W. Hansen, W. F. Holmgren, A. R. Jensen, M. A. Mikofski, and A. Driesse, "pvlib python: 2023 project update," *J. Open Source Softw.*, vol. 8, no. 92, p. 5994, Dec. 2023, doi: 10.21105/joss.05994.
[51] R. Perez, R. Seals, P. Ineichen, R. Stewart, D. Menicucci, A new simplified version of the perez diffuse irradiance model for tilted surfaces, Sol. Energy 39 (3) (1987) 221–231, https://doi.org/10.1016/S0038-092X(87)80031-2.
[52] R. Perez, R. Stewart, R. Seals, T. Guertin, "The development and verification of the Perez diffuse radiation model," Albuquerque, NM, and Livermore, CA (United States) (1988), https://doi.org/10.2172/7024029.
[53] R. Perez, P. Ineichen, R. Seals, J. Michalsky, R. Stewart, Modeling daylight availability and irradiance components from direct and global irradiance, Sol. Energy 44 (5) (1990) 271–289, https://doi.org/10.1016/0038-092X(90)90055-H.
[54] T. Huld, R. Müller, A. Gambardella, A new solar radiation database for estimating PV performance in Europe and Africa, Sol. Energy 86 (6) (2012) 1803–1815, https://doi.org/10.1016/j.solener.2012.03.006.
[55] C. D. Rodríguez-Gallegos, O. Gandhi, H. Sun, C. Paton, J. Zhang, J. Moideen Yacob Ali, M. S. Alvarez-Alvarado, W. Zhang, C. A. Rodríguez-Gallegos, L. H. C. Chua, and T. Reindl, "Global floating PV status and potential," *Progress in Energy*, vol. 7, no. 1, p. 015001, Jan. 2025, doi: 10.1088/2516-1083/ad9074.
[56] F. Bauelos-Ruedas, C. Angeles-Camacho, and Sebastin, "Methodologies Used in the Extrapolation of Wind Speed Data at Different Heights and Its Impact in the Wind Energy Resource Assessment in a Region," in *Wind Farm - Technical Regulations, Potential Estimation and Siting Assessment*, no. June 2011, InTech, 2011. doi: 10.5772/20669.
[57] T. Huld, A. Amillo, Estimating PV module performance over large geographical regions: the role of irradiance, air temperature, wind speed and solar spectrum, Energies (Basel) 8 (6) (2015) 5159–5181, https://doi.org/10.3390/en8065159.
[58] A. Livera, M. Theristis, E. Koumpli, S. Theocharides, G. Makrides, J. Sutterlueti, J. S. Stein, G.E. Georghiou, Data processing and quality verification for improved photovoltaic performance and reliability analytics, Prog. Photovolt. Res. Appl. 29 (2) (2021) 143–158, https://doi.org/10.1002/pip.3349.
[59] International Electrotechnical Commission (IEC), "IEC 61724-1 Photovoltaic system performance - Part 1: Monitoring," 2021.
[60] E. H. Wong, Y. C. Teo, and T. B. Lim, "Moisture diffusion and vapour pressure modeling of IC packaging," in *1998 Proceedings. 48th Electronic Components and Technology Conference (Cat. No.98CH36206)*, IEEE, 1998, pp. 1372–1378. doi: 10.1109/ECTC.1998.678922.
[61] S. Mitterhofer, J. Slapšak, A. Astigarraga, D. Moser, G. O. Hernandez, P. V. Chiantore, W. Luo, Y. S. Khoo, J. Rabanal-Arabach, E. Fuentealba, P. Ferrada, M. Trigo Gonzalez, J. Ascencio-Vásquez, M. Topič, and M. Jankovec, "Measurement and Simulation of Moisture Ingress in PV Modules in Various Climates," *IEEE J. Photovolt.*, vol. 14, no. 1, pp. 140–148, Jan. 2024, doi: 10.1109/JPHOTOV.2023.3323808.
[62] D. Mortensen, D. Lindholm, K. Friestad, B.R. Henriksen, H.G. Fjær, M. Rudshaug, E. A. Sørheim, Crystallization furnace modeling including coupled heat and fluid flow, stresses and deformations, Energy Procedia 38 (2013) 597–603, https://doi.org/10.1016/j.egypro.2013.07.322.
[63] M. Kempe, S. Ovaitt, M. Springer, T. Ford, and J. Karas, "The 'PVLib' of Degradation: PVDEG," in *PVPMC*, 2024.
[64] R.I. Woolway, I.D. Jones, D.P. Hamilton, S.C. Maberly, K. Muraoka, J.S. Read, R. L. Smyth, L.A. Winslow, Automated calculation of surface energy fluxes with high-frequency lake buoy data, Environ. Model. Software 70 (2015) 191–198, https://doi.org/10.1016/j.envsoft.2015.04.013.
[65] X. Zeng, M. Zhao, R.E. Dickinson, Intercomparison of bulk aerodynamic algorithms for the computation of sea surface fluxes using TOGA COARE and TAO data, J. Clim. 11 (10) (1998) 2628–2644, https://doi.org/10.1175/1520-0442(1998)011<2628:IOBAAF>2.0.CO;2.
[66] E.T. Crosman, J.D. Horel, Sea and lake breezes: a review of numerical studies, Boundary Layer Meteorol. 137 (1) (2010) 1–29, https://doi.org/10.1007/s10546-010-9517-9.

[67] R. Asadpour, M.T. Patel, S. Clark, N. Bosco, T. Silverman, M.A. Alam, Worldwide physics-based lifetime prediction of c-si modules due to solder-bond failure, IEEE J. Photovolt. 12 (2) (2022) 533–539, https://doi.org/10.1109/JPHOTOV.2021.3136164.

[68] R.I. Woolway, G. Zhao, S.M.G. Rocha, S.J. Thackeray, A. Armstrong, Decarbonization potential of floating solar photovoltaics on lakes worldwide, Nat. Water 2 (6) (2024) 566–576, https://doi.org/10.1038/s44221-024-00251-4.

[69] D. Lindholm, J. Selj, T. Kjeldstad, H. Fjær, V. Nysted, CFD modelling to derive U-values for floating PV technologies with large water footprint, Sol. Energy 238 (2022) 238–247, https://doi.org/10.1016/j.solener.2022.04.028.

[70] N. M. Silvério, R. M. Barros, G. L. Tiago Filho, M. Redón-Santafé, I. F. S. dos Santos, and V. E. de M. Valério, "Use of floating PV plants for coordinated operation with hydropower plants: Case study of the hydroelectric plants of the São Francisco River basin," *Energy Convers. Manag.*, vol. 171, pp. 339–349, Sep. 2018, doi: 10.1016/j.enconman.2018.05.095.

[71] N. Roosloot, J.H. Selj, G. Otnes, Evaluating durability of a double edge sealant in a floating photovoltaic application, IEEE J. Photovolt. 14 (5) (2024) 785–792, https://doi.org/10.1109/JPHOTOV.2024.3417420.

[72] M.D. Kempe, A.A. Dameron, M.O. Reese, Evaluation of moisture ingress from the perimeter of photovoltaic modules, Prog. Photovolt. Res. Appl. 22 (11) (2014) 1159–1171, https://doi.org/10.1002/pip.2374.

[73] N. Roosloot, B. A. Denfeld, C. DeGasperi, P. Verburg, H. Yao, and J. A. Rusak, "Data used in 'Comparison of Humidity-Induced Stress Levels between Floating and Ground-Mounted Photovoltaics' (Version 1.0)." Zenodo, 2025. doi: 10.5281/zenodo.16269732.

[74] IEA PVPS Task 13, "Translation Tool for Geo Data to Koeppen-and-Geiger-Climate-Zone." Accessed: Nov. 14, 2024. [Online]. Available: https://iea-pvps.org/wp-content/uploads/2020/03/191021_Translation_Koeppen_and_Geiger_climate_zone.xlsx.